

# Learning-based Feedback Controller for Deformable Object Manipulation

Biao Jia\*, Zhe Hu\*, Zherong Pan, Dinesh Manocha, Jia Pan

**Abstract**—In this paper, we present a general learning-based framework to automatically visual-servo control the position and shape of a deformable object with unknown deformation parameters. The servo-control is accomplished by learning a feedback controller that determines the robotic end-effector’s movement according to the deformable object’s current status. This status encodes the object’s deformation behavior by using a set of observed visual features, which are either manually designed or automatically extracted from the robot’s sensor stream. A feedback control policy is then optimized to push the object toward a desired featured status efficiently. The feedback policy can either be learned online or offline. Our online policy learning is based on the Gaussian Process Regression (GPR), which can achieve fast and accurate manipulation and is robust to small perturbation. An offline imitation learning framework is also proposed to achieve a control policy that is robust to large perturbation in the human-robot interaction. We validate the performance of our controller on a set of deformable object manipulation tasks and demonstrate that our method can achieve effective and accurate servo-control for general deformable objects with a wide variety of goal settings. Experiment videos are available at <https://sites.google.com/view/mso-fogpr>.

## I. INTRODUCTION

Robot manipulation has been extensively studied for decades and there is extensive work on the manipulation of rigid and deformable objects. Compared to the manipulation of a rigid object, the state of which can be completely described by a six-dimensional configuration space, deformable object manipulation (DOM) is more challenging due to its very high configuration space dimensionality. The resulting manipulation algorithm needs to handle this dimensional complexity and maintain the tension to perform the task. DOM has many important applications, including cloth folding [1], [2], robot-assisted dressing or household chores [3], [4], ironing [5], coat checking [6], sewing [7], string insertion [8], robot-assisted surgery and suturing [9], [10], and transporting large materials like cloth, leather, and composite materials [11].

There are two main challenges that arise in performing DOM tasks. First, we need to model a feature representation of the object status, that can account for the object’s possibly large deformations. The design of such feature is usually task-dependent and object-specific. For instance, a cloth needs richer features than a rope, and a surgical-related application requires more sophisticated features than a consumer application. As a result, feature design is usually a tedious

Biao Jia, Zherong Pan, and Dinesh Manocha are with the Department of Computer Science, The University of North Carolina, Zhe Hu and Jia Pan are with the Department of Mechanical and Biomedical Engineering, City University of Hong Kong.

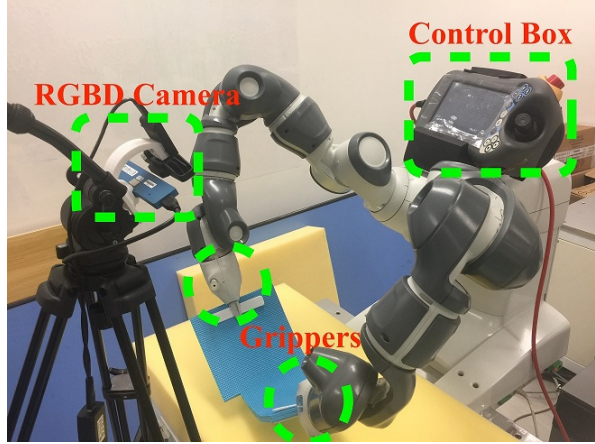


Fig. 1: Our robotic system for deformable object manipulation is made by two 3D cameras and one dual-arm ABB robot.

manual procedure. Second, we need to develop a controller that maps the object’s state features to a robot control action in order to achieve a specific task. The design of such a controller is usually also task-dependent. For instance, a manipulation controller for human dressing will require a more expressive controller parametrization than that needed to flatten a piece of paper. As a result, controller design usually requires tedious manual parameter tuning when generalizing to different tasks. More importantly, the two problems of feature extraction and controller design were solved as two separate problems. With the recent development of deep (reinforcement) learning, a prominent method [12], [13] is to represent feature extraction and controller parametrization as two neural networks, which are either trained jointly or separately. However, the design decisions for these two networks, e.g., their network structures, are made independently. This method suffers from the large number of parameters need to be manually determined. There are some more task-specific methods, such as [5], [14], which use a vision-based feature extractor but the controller is a standalone optimization-based motion planner whose formulation is independent of feature extraction. These methods are hard to extend because the feature-based objective functions for trajectory optimization are task-specific.

To solve above challenges, there is rich literature on autonomous robotic DOM, and these work can be classified into three categories. The first group of approaches require a physical model about the object’s deformation properties in terms of stiffness, Young’s modulus, or FEM coefficients, to design a control policy [9], [15]–[19]. However, such defor-

mation parameters are difficult to be estimated accurately and may even change during the manipulation process, especially for objects made by nonlinear elastic or plastic materials. The second group of approaches use manually designed low-dimensional features to model the object's deformation behavior [17], [18], [20], [21] and then use adaptive linear controller to accomplish the task. The final group of approaches do not explicitly model the deformation parameters of the object. Instead, they use vision or learning methods to accomplish tasks directly [1], [10], [14], [22]–[26]. These methods focus on high-level policies but lack the capability to achieve accurate operations – actually their success rate is low and some of them are open-loop methods. As a result, how to design appropriate features and controllers to achieve accurate and flexible deformable object manipulation is still an open research problem in robotics [27].

In this paper, we focus on designing a general learning-based feedback control framework for accurate and flexible DOM. The feedback controller's input is a feature representation for the deformable object's current status, and its output is the robotic end-effector's movement. Our framework provides solutions to both the feature design and controller parameterization challenges. For feature design, we propose both a set of manually designed low-level features and a novel higher-level feature based on a histogram of oriented wrinkles, which is automatically extracted from data to describe the shape variation of a highly deformable object. For controller parameterization, we first propose a novel nonlinear feedback controller based on Gaussian Process Regression (GPR), which online learns the object's deformation behavior and is able to accomplish a set of challenging DOM tasks accurately and reliably. We further design a controller which treat feature extraction and controller design as a coupled problem by using a random forest trained using two-stage learning. During the first stage, we construct a random forest to classify a sampled dataset of images of deformable objects. Based on the given forest topology, we augment the random forest by defining one optimal control action for each leaf-node, which provides the action prediction for any unseen image that falls in that leaf-node. In this way, the feature extraction helps determine the parameterization of the controller. The random forest construction and controller optimization are finally integrated into an imitation learning framework to improve the robustness of human-robot co-manipulation tasks.

We have integrated our approach with an ABB YuMi dual-arm robot and a camera for image capture and used it to manipulate different cloth materials for different tasks. We highlight the real-time performance of our method on a set of DOM benchmarks, including standard feature point reaching tasks (as in [17], [18]), the tasks for cloth stretching, folding, twisting, and placement, and the industrial tasks for cloth assembly. Our manipulation system successfully and efficiently accomplishes these manipulation tasks for a wide variety of objects with different deformation properties.

Our main contributions in this paper include:

- A general feedback control framework for DOM tasks.

- A set of manually designed low-level features that work well in a set of challenging DOM tasks.
- A novel histogram feature representation of highly deformable materials (HOW-features) that are computed directly from the streaming RGB data using Gabor filters. These features are then correlated using a sparse representation framework in terms of a visual feedback dictionary and then fed to the feedback controller to generate appropriate robot actions.
- An online Gaussian Process Regression based nonlinear feedback controller for DOM task which is robust and adaptive to the object's unknown deformation parameters.
- A random-forest-based DOM-controller parametrization which is robust and less parameter-sensitive; an imitation learning algorithm based framework that trains robust DOM controller using a deformable object simulator.
- A set of benchmark DOM tasks that have importance for manufacturing or service industry.

The rest of this paper is organized as follows. We briefly survey the related works in Section II. We give an overview about our DOM framework in Section III. We present the details of our feature design and extraction in Section IV. We discuss the details of our new controllers in Section VI. Finally, demonstrate the performance of our new approach with a set of experiments on a wide variety of soft objects in Section VIII with conclusions in Section IX.

## II. RELATED WORK

### A. Deformable object manipulation

Many robotic manipulation method for deformable objects have been proposed recent years. Early work [28], [29] used knot theory or energy theory to plan the manipulation trajectories for linear deformable objects like ropes. Some recent work [30] further considered manipulating cloths using dexterous cloths. These work required a complete and accurate knowledge about the object' geometric and deformation parameters and thus are not applicable in practice.

More practical work used sensors to guide the manipulation process. [31] used image to estimate the knot configuration. [1] used vision to estimate the configuration of a cloth and then leverage gravity to accomplish folding tasks [32]. [6] used RGBD camera to identify the boundary components in clothes. [14], [33] first used vision to determine the status of the cloth, then optimized a set of grasp points to unfold the clothes on the table, and finally found a sequence of folding actions. Schulman *et al.* [10] enabled a robot to accomplish complex multi-step deformation object manipulation strategies by learning from a set of manipulation sequences with depth images to encode the task status. Such learning from demonstration technique has further been extended using reinforcement learning [22] and tangent space mapping [23]. A deep learning-based end-to-end framework has also been proposed recently [24]. A complete pipeline for clothes folding task including vision-

based garments grasping, clothes classification and unfolding, model matching and folding has been described in [25].

Above methods generally did not explicitly model the deformation parameters of the deformation objects, which is necessary for high-quality manipulation control. Some methods used uncertainty model [15] or heuristics [8], [34] to take into account rough deformation models during the manipulation process. Some work required an offline procedure to estimate the deformation parameters [16]. There are several recent work estimating the object's deformation parameters in an online manner and then design controller accordingly. Navarro-Alarcon *et al.* [17], [18], [21] used an adaptive and model-free linear controller to servo-control soft objects, where the object's deformation is modeled using a spring model [35]. [19] learned the models of the part deformation depending on the end-effector force and grasping parameters in an online manner to accomplish high-quality cleaning task. A more complete survey about deformable object manipulation in industry is available in [27].

### B. Deformable object feature design

Different techniques have been proposed for motion planning for deformable objects. Most of works on deformable object manipulation focus on volumetric objects such as a deforming ball or linear deformable objects such as steerable needles [28], [36]–[38]. By comparison, cloth-like thin-shell objects tend to exhibit more complex deformations, forming wrinkles and folds. Current solutions for thin-shelled manipulation problems are limited to specific tasks, including folding [14], ironing [5], sewing [7], and dressing [39]. On the other hand, deformable body tracking solves a simpler problem, namely inferring the 3D configuration of a deformable object from sensing inputs. There is literature on deformable body tracking, which deals with inferring the 3D configuration from sensor data [40]–[42]. However, these methods usually require a template mesh to be known as a priori, and the allowed deformations are relatively small. Recently, some template-less approaches are also proposed, which tackle the tracking and reconstruction problems jointly in real-time, including [43]–[45].

Rather than requiring a complete 3D reconstruction of the entire object, a visual-servo controller only uses single-view observations about the object as the input. However, even the single-view observation is high-dimensional. Thus, previous DOM methods use various feature extraction and dimensionality-reduction techniques, including SIFT-features [14], and combined depth and curvature-based features [25], [46]. Recently, deep neural-networks became a mainstream general-purpose feature extractor. They have also been used for manipulating low-DOF articulated bodies [12] and DOM applications [47]. However, visual feature extraction is always decoupled from controller design in all these methods.

### C. Deformable object controller optimization

In robotics, reinforcement learning [48], imitation learning [49], and trajectory optimization [50] have been used to compute optimal control actions. Trajectory optimization, or a model-based controller, has been used in [5], [14], [51] for DOM applications. Although they are accurate, these methods cannot achieve real-time performance. For low-DOF robots such as articulated bodies [52], researchers have developed real-time trajectory optimization approaches, but it is hard to extend them to deformable models due to the high simulation complexity of such models. Currently, real-time performance can only be achieved by learning-based controllers [46], [47], [53], which use supervised learning to train real-time controllers. However, as pointed out in [54], these methods are not robust in handling unseen data. Therefore, we are able to further improve the robustness by using imitation learning. [55] used reinforcement learning to control a soft-hand but the object to be manipulated by the soft-hand was still rigid.

DOM controller design is dominated by Visual servoing techniques [56], [57], which aim at controlling a dynamic system using visual features extracted from images. They have been widely used in robotic tasks like manipulation and navigation. Recent work includes the use of histogram features for rigid objects

The dominating approach for DOM tasks is visual servoing techniques [56], [57] aim at controlling a dynamic system using visual features extracted from images. They have been widely used in robotic tasks like manipulation and navigation. Recent work includes the use of histogram features for rigid objects [58]. Sullivan *et al.* [20] use a visual servoing technique to solve the deformable object manipulation problem using active models. Navarro-Alarcon *et al.* [17], [18], [21] use an adaptive and model-free linear controller to servo-control soft objects, where the object's deformation is modeled using a spring model [35]. Langsfeld *et al.* [19] perform online learning of part deformation models for robot cleaning of compliant objects. Our goal is to extend these visual servoing methods to perform complex tasks on highly deformable materials.

## III. OVERVIEW AND PROBLEM FORMULATION

The problem of 3D deformable object manipulation can be formulated as follows. Similar to [35], we describe an object as a set of discrete points, which are classified into three types: the manipulated points, the feedback points, and the uninformative points, as shown in Figure 2. The manipulated points correspond to the positions on the object that are grabbed by the robot and thus is fixed relative to the robotic end-effectors; the feedback points correspond to the object surface regions that define the task goal setting and involve in the visual feedbacks; and the uninformative points correspond to other regions on the object. Given this setup, the deformable object manipulation problem is about how to move the manipulated points in order to drive the feedback points toward a required target configuration.

Symbol	Meaning
$\mathcal{C}$	3D configuration space of the object
$c$	a configuration of the object, $c = \{\mathbf{p}\} \cup \{\mathbf{q}\} \cup \{\mathbf{r}\}$
$\mathbf{p}$	feedback feature points on the object
$\mathbf{q}$	uninformative points on the object
$\mathbf{r}$	robot end-effectors' grasping points on the object
$\mathcal{O}(c)$	an observation of object
$\mathbf{s}$	the feature vector extracted from $\mathcal{O}(c)$
$\mathbf{c}^*$	target configuration of the object
$\mathbf{r}^*$	optimal grasping points returned by the expert
$H$	interaction function linking velocities of the feature space to the end-effector configuration space
$\text{dist}_s$	distance measure in the feature space
$\text{dist}_\pi$	distance measure in the policy space
$\pi$	DOM-control policy
$\alpha$	random forest topology
$\beta$	controller parameters
$\gamma$	confidence of leaf-node
$\theta$	parameter sparsity
$K$	the number of decision trees
$l_k$	a leaf-node of $k$ -th decision tree
$l_k(\mathcal{O}(c))$	the leaf-node that $\mathcal{O}(c)$ belongs to
$\mathcal{L}$	labeling function for optimal actions
$\mathcal{F}$	feature transformation for observation

TABLE I: Symbol table.

Our goal is to optimize a realtime feedback controller to deform the object into a desired target configuration. We denote the 3D configuration space of the object as  $\mathcal{C}$ . Typically, a configuration  $c \in \mathcal{C}$  can be discretely represented as a 3D mesh of the object and the dimension of  $\mathcal{C}$  can be several thousands. However, we assume that only a partial observation  $\mathcal{O}(c)$  is known, which in our case is an RGB-D image from a single, fixed point of view.

Since the manipulation of deformable object is usually executed at a low speed to avoid vibration, we can reasonably assume that the object always lies in the quasi-static state where the internal forces caused by the elasticity of the object is balanced with the external force applied by the end-effector on the manipulated points. We use a potential energy function  $U(\mathbf{p}, \mathbf{q}, \mathbf{r})$  to formulate the elasticity of the deformable object, where the potential energy depends on all the points on the object, and vectors  $\mathbf{p}$ ,  $\mathbf{q}$  and  $\mathbf{r}$  represent the stacked coordinates of all feedback points, uninformative points, and manipulated points, respectively. The equation of equilibrium for the object can then be described as follows:

$$\frac{\partial U}{\partial \mathbf{p}} = \mathbf{0}, \quad (1)$$

$$\frac{\partial U}{\partial \mathbf{q}} = \mathbf{0}, \quad (2)$$

$$\frac{\partial U}{\partial \mathbf{r}} - \mathbf{F} = \mathbf{0}, \quad (3)$$

where  $\mathbf{F}$  is the external force vector applied on the manipulated points. To solve the above equations, we need exact knowledge about that deformable object's deformation property, which is not available or difficult to acquire in many applications. To cope with this issue, we first simplify the potential energy function to only depend on  $\mathbf{p}$  and  $\mathbf{r}$ , which is reasonable because usually the uninformative points are far

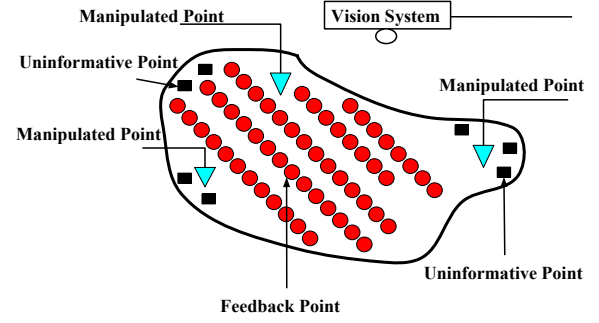


Fig. 2: We model a soft object using three classes of points: manipulated points  $\mathbf{r}$ , feedback points  $\mathbf{p}$ , and uninformative points  $\mathbf{q}$ .

from the manipulated and feedback points and thus their influence on the manipulation process is small and can be neglected. Next, we perform Taylor expansion of Equation 3 and Equation 1 about the current static equilibrium status  $(\bar{\mathbf{p}}, \bar{\mathbf{r}})$ , and the equation of equilibrium implies a relationship between the relative displacements of feedback points and the manipulated points:

$$A(\delta\mathbf{p}) + B(\delta\mathbf{r}) = \mathbf{0}, \quad (4)$$

where  $\delta\mathbf{p} = \mathbf{p} - \bar{\mathbf{p}}$  and  $\delta\mathbf{r} = \mathbf{r} - \bar{\mathbf{r}}$  are the displacement relative to the equilibrium for feedback points and manipulated points, respectively. The functions  $A(\cdot)$  and  $B(\cdot)$  are non-linear in general, though they can be linear in some special cases. For instance, when only performing the first order Taylor expansion as what is done in [18],  $A(\delta\mathbf{p}) = \frac{\partial^2 U}{\partial \mathbf{r} \partial \mathbf{p}}$  and  $B(\delta\mathbf{r}) = \frac{\partial^2 U}{\partial (\mathbf{r})^2} \delta\mathbf{r}$  are two linear functions. In this paper, we allow  $A(\cdot)$  and  $B(\cdot)$  to be general functions to estimate a better model for the deformable object manipulation process.

We further assume the function  $B(\cdot)$  to be invertible, which implies

$$\delta\mathbf{r} = D(\delta\mathbf{p}), \quad (5)$$

where  $D = A \circ B^{-1}$  is the mapping between the velocities of the feedback points and the manipulated points. In this way, we can determine a suitable end-effector velocity via feedback control  $\delta\mathbf{r} = D(\eta \cdot \Delta\mathbf{p})$  to derive the object toward its goal state, where  $\Delta\mathbf{p} = \mathbf{p}^* - \mathbf{p}$  is the difference between the desired vector  $\mathbf{p}^*$  and the current vector of the feedback points and  $\eta$  is the feedback gain.

However, the velocities of feedback points usually cannot be directly used in the control, because in practice these velocities are measured using visual tracking of deformable objects and thus are likely to be noisy or even unreliable when tracking fails. More importantly, a soft object needs a large set of feedback points to characterize its deformation, but a robotic manipulation system usually only has a few end-effectors, and thus the  $D(\cdot)$  function in Equation 5 is a mapping from the high-dimensional space of feedback point velocities to the low-dimensional space of manipulated point velocities. Such a system is extremely underactuated and thus the convergence speed of the control would be slow.

To deal with aforementioned difficulties, we replace the feedback points  $\mathbf{p}$  by a low-dimensional feature vector  $\mathbf{s} = C(\mathbf{p})$  extracted from the observed part of the deformable object, where  $C(\cdot)$  is the feature extraction function. Around the equilibrium state, we have  $\delta\mathbf{s} = C'(\bar{\mathbf{p}})\delta\bar{\mathbf{p}}$ , and can rewrite the equilibrium function using the feature vector as

$$\delta\mathbf{r} = D(C'(\bar{\mathbf{p}})^{-1}\delta\mathbf{s}) \triangleq H(\delta\mathbf{s}), \quad (6)$$

where the function  $H(\cdot)$  is called the **interaction function**.

The manipulation problem of deformable object can finally be described as: given the desired state  $\mathbf{s}^*$  of an object in the feature space, design a controller which learns the interaction function  $H(\cdot)$  in an offline or online manner, and outputs the control velocity  $\delta\mathbf{r}$  decreasing the distance between  $\mathbf{s}$  and  $\mathbf{s}^*$ , which are the object's current state and desired goal state in the feature space. More formally, the controller is:

$$\delta\mathbf{r} = H(\eta \cdot \mathbf{dist}_s(\mathbf{s}, \mathbf{s}^*)), \quad (7)$$

where  $\mathbf{dist}_s$  is the distance metric in the feature space and  $\eta$  is the feedback gain. If we assume  $H$  to be a linear function and  $\mathbf{dist}_s$  to be a linear metric, then the controller degrades to the linear visual servo controller:

$$\delta\mathbf{r} = \eta \cdot (\mathbf{s} - \mathbf{s}^*). \quad (8)$$

In addition, since  $\delta\mathbf{r} = \mathbf{r} - \bar{\mathbf{r}}$  and  $\bar{\mathbf{r}}$  is usually a known vector, we can also write the controller as a policy  $\pi$ :

$$\mathbf{r} = H(\eta \cdot \mathbf{dist}_s(\mathbf{s}, \mathbf{s}^*)) + \bar{\mathbf{r}} = \pi(\mathbf{s} | \mathcal{O}(c)), \quad (9)$$

where  $\mathcal{O}(c)$  is the observation about the current state of the deformable object and is equivalent to  $\mathbf{s}$ . This form is more popular in the policy optimization literature.

#### IV. FEATURE EXTRACTION: MANUAL DESIGN

For rigid body manipulation, an object's state can be completely described by its centroid position and orientation. But such global features are not sufficient to determine the configuration of a deformable object. As mentioned in Section III, we extract a feature vector  $\mathbf{s}$  from the observed feedback points to represent the object's state. One common practice for feature extraction is to manually design task-dependent features. Here we present a set of features that are able to provide high-quality representations for DOM tasks, as will be demonstrated in our experiments.

##### A. Global features

1) *Centroid*: The centroid feature  $\mathbf{c} \in \mathcal{R}^3$  is computed as the geometric center of the 3D coordinates of all the observed feedback points:

$$\mathbf{c} = (\mathbf{p}_1 + \mathbf{p}_2 + \cdots + \mathbf{p}_K) / K. \quad (10)$$

2) *Positions of feedback points*: Another way to describe a deformable object's configuration is to directly use the positions of all observed feedback points as part of  $\mathbf{x}$ , i.e.

$$\rho = [(\mathbf{p}_1)^T, (\mathbf{p}_2)^T, \dots, (\mathbf{p}_K)^T] \quad (11)$$

##### B. Local features

1) *Distance between points*: The distance between each pair of feedback points intuitively measures the stretch of deformable objects. This feature is computed as

$$d = \|\mathbf{p}_1 - \mathbf{p}_2\|^2, \quad (12)$$

where  $\mathbf{p}_1$  and  $\mathbf{p}_2$  are a pair of feedback points.

2) *Surface variation indicator*: For deformable objects with developable surfaces, the surface variation around each feedback point can measure the local geometric property. Given a feedback point  $\mathbf{p}$ , we can compute the covariance matrix  $\Omega$  for its neighborhood and then the surface variation  $\sigma$  is computed as

$$\sigma = \frac{\lambda_0}{\lambda_0 + \lambda_1 + \lambda_2} \quad (13)$$

where  $\lambda_0, \lambda_1, \lambda_2$  are eigenvectors of  $\Omega$  with  $\lambda_0 \leq \lambda_1 \leq \lambda_2$ .

3) *Extended FPFH from VFH*: Extended FPFH is the local descriptor of VFH and is based on Fast Point Feature Histograms (FPFH) [59]. Its idea is to use a histogram to record differences between the centroid point  $\mathbf{p}_c$  and its normal  $\mathbf{n}_c$  with all other points and normals.

##### C. Feature selection for different tasks

According to our experience, for 1D deformable objects such as rope, we can use centroid, distance or the coordinates of several marked points; for 2D deformable objects like deformable sheets, surface variation indicator or extended FPFH are more effective to represent the states of the deformable objects. The features such as centroid and distance are also used in [18], and thus we will use these features to compare our method with [18]. Our learning-based controllers discussed later are not very sensitive to the feature selection because they can adaptively weight the importance of different features. Nevertheless, we can introduce task-relevant prior knowledge into the controller by manually designing task-specific features, which would be helpful to the robustness and effectiveness of the controlling process.

#### V. FEATURE EXTRACTION: DATA-DRIVEN DESIGN

Manual feature design is tedious and cannot be optimized for a given task. Here, we present a novel feature representation, a Histogram of Oriented Wrinkles (HOW), to describe the shape variation of a highly deformable object like clothes. These features are computed by applying Gabor filters and extracting the high-frequency and low-frequency components. We precompute a visual feedback dictionary using an offline training phase that stores a mapping between these visual features  $\mathbf{s}$  and the velocity of the end-effector  $\delta\mathbf{r}$ . At runtime, we automatically compute the goal configurations based on the manipulation task and use sparse linear representation to compute the velocity of the controller from the dictionary.

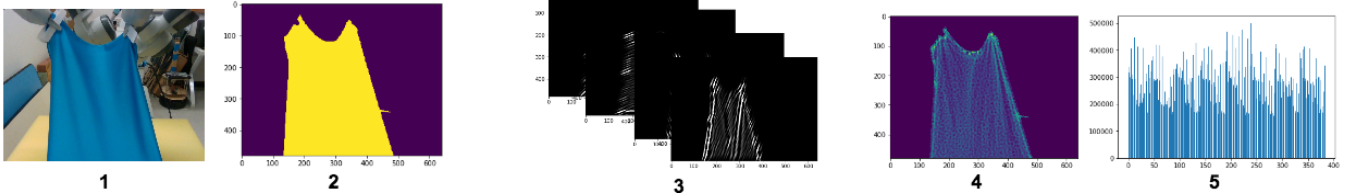


Fig. 3: Pipeline for HOW-feature computation: Given the input image (1), we use the following stages: (2) foreground segmentation using Gaussian mixture; (3) image filtering with multiple orientations and wavelengths of Gabor Kernel; (4) discretization of the filtered images to form grids of histogram; (5) stacking the feature matrix to a single column vector.

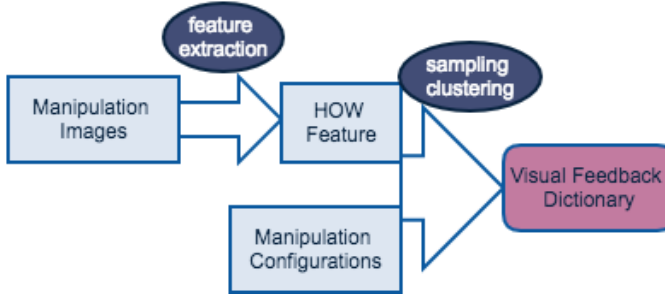


Fig. 4: Computing the visual feedback dictionary: The input to this offline process is the recorded manipulation data with images and the corresponding configuration of the robot's end-effector. The output is a visual feedback dictionary, which links the velocity of the features and the controller.

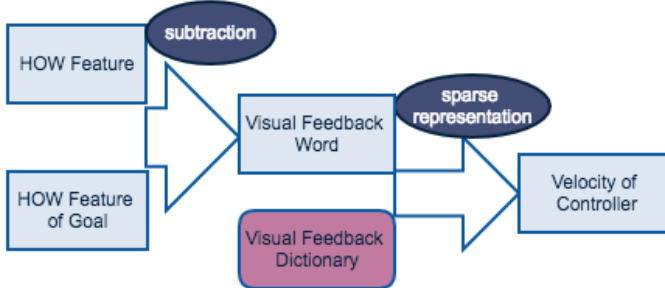


Fig. 5: At runtime, the controller leverages the HOW features in two stages. First, we extract HOW features from the visual input and compute the visual feedback word by subtracting the extracted features from the features of the goal configuration. Then, we apply the sparse representation and compute the velocity of the controller for manipulation.

#### A. Histogram of deformation model feature

Here we present our algorithm to compute the HOW features from the camera stream. These are low-dimensional features of the highly deformable material.

The pipeline of our HOW-feature computation process is shown in Figure 3, which have three stages as follows.

1) *Foreground segmentation*: To find the foreground partition of a deformable object, we apply the Gaussian mixture algorithm [60] on the RGB data captured by the camera. The intermediate result of segmentation is shown in Figure 3(2).

2) *Deformation enhancement*: To model the high dimensional characteristics of the highly deformable material, we use deformation enhancement. This is based on the perceptual observation that most deformations can be modeled

by shadows and shape variations. Therefore, we extract the features corresponding to shadow variations by applying a Gabor transform [61] to the RGB image. This results in the enhancement of the ridges, wrinkles, and edges (as shown in Figure 3). We convolve the  $N$  deformation filters  $\{d_i\}$  to the image  $I$  and represent the result as  $\{d_i(I)\}$ .

In the spatial domain, a 2D Gabor filter is a Gaussian kernel function modulated by a sinusoidal plane wave [62] and it has been used to detect wrinkles [63]. The 2D Gabor filter can be represented as follows:

$$g(x, y; \lambda, \theta, \phi, \sigma, \gamma) = \exp\left(-\frac{x'^2 + \gamma^2 y'^2}{2\sigma^2}\right) \sin\left(2\pi \frac{x'}{\lambda} + \phi\right), \quad (14)$$

where  $x' = x \cos \theta + y \sin \theta$ ,  $y' = -x \sin \theta + y \cos \theta$ ,  $\theta$  is the orientation of the normal to the parallel stripes of the Gabor filter,  $\lambda$  is the wavelength of the sinusoidal factor,  $\phi$  is the phase offset,  $\sigma$  is the standard deviation of the Gaussian, and  $\gamma$  is the spatial aspect ratio. When we apply the Gabor filter to our deformation model image, the choice of wavelength ( $\lambda$ ) and orientation ( $\theta$ ) are the key parameters with respect to the wrinkles of deformable materials. As a result, the deformation model features consist of multiple Gabor filters ( $d_1, \dots, n(I)$ ) with different values of wavelengths ( $\lambda$ ) and orientations ( $\theta$ ).

3) *Grids of histogram*: A histogram-based feature is an approximation of the image which can reduce the data redundancy and extract a high-level representation that is robust to local variations in an image. Histogram-based features have been adopted to achieve a general framework for photometric visual servoing [58]. Although the distribution of the pixel value can be represented by a histogram, it is also significant to represent the position in the feature space of the deformation to achieve the manipulation task. Our approach is inspired by the study of grids of Histogram of Oriented Gradient [64], which is computed on a dense grid of uniformly spatial cells.

We compute the grids of histogram of deformation model feature by dividing the image into small spatial regions and accumulating local histogram of different filters ( $d_i$ ) of the region. For each grid, we compute the histogram in the region and represent it as a matrix. We vary the grid size and compute matrix features for each size. Finally, we represent the entries of a matrix as a column feature vector. The complete feature extraction process is described in Algorithm 1.

---

**Algorithm 1** Computing HOW features

---

**Input:** image  $I$  of size  $(w_I, h_I)$ , deformation filtering or Gabor kernels  $\{d_1 \dots d_{N_d}\}$ , grid size set  $\{g_1, \dots, g_{N_g}\}$ .

**Output:** feature vector  $s$

- 1: **for**  $i = 1, \dots, N_d$  **do**
- 2:   **for**  $j = 1, \dots, N_g$  **do**
- 3:     **for**  $(w, h) = (1, 1), \dots, (w_I, h_I)$  **do**
- 4:       ▷ compute the indices using truncation
- 5:        $(x, y) = (\text{TRUNC}(w/g_j), \text{TRUNC}(h/g_j))$
- 6:       ▷ add the filtered pixel value to the specific bin of the grid
- 7:        $s_{i,j,x,y} = s_{i,j,x,y} + d_i(I(w, h))$
- 8:     **end for**
- 9:   **end for**
- 10: **end for**
- 11: **return**  $s$

---

The HOW-feature has several advantages. It captures the deformation structure, which is based on the characteristics of the local shape. Moreover, it uses a local representation that is invariant to local geometric and photometric transformations. This is useful when the translations or rotations are much smaller than the local spatial or orientation grid size.

### B. Manipulation using visual feedback dictionary

Here we present our algorithm for computing the visual feedback dictionary. At runtime, this dictionary is used to compute the corresponding velocity ( $\Delta r$ ) of the controller based on the visual feedback ( $\Delta s(I)$ ).

1) *Building visual feedback dictionary:* As shown in Figure 4, the inputs of the offline training phase are a set of images and end-effector configurations ( $\{I^{(t)}\}$ ,  $\{r^{(t)}\}$ ) and the output is the visual feedback dictionary ( $\{\{\Delta s^{(i)}\}, \{\Delta r^{(i)}\}\}$ ).

For the training process, the end-effector configurations, ( $\{r^{(t)}\}$ ), are either collected by human tele-operation or generated randomly. A single configuration ( $r^{(i)}$ ) of the robot is a column vector of length  $N_{dof}$ , the number of degrees-of-freedom to be controlled.  $r \in \mathbb{R}^{N_{dof}}$  and its value is represented in the configuration space.



Fig. 6: Visual feedback dictionary: The visual feedback word is defined by the difference between the visual features  $\Delta s = s - s^*$  and the controller positions  $\Delta r = r - r^*$ . The visual feedback dictionary  $\{\{\Delta s^{(i)}\}, \{\Delta r^{(i)}\}\}$  consists of visual feedback words computed. We show the initial and final states on the left and right, respectively.

In order to compute the mapping  $H(\cdot)$  in Equation 6 from the visual feedback to the velocity, we need to transform the configurations  $\{r^{(t)}\}$  and image stream  $\{I^{(t)}\}$  into velocities  $\{\Delta r^{(t)}\}$  and the visual feature feedback  $\{\Delta s^{(t)}\}$ . One solution is to select a fixed time step  $\Delta t$  and to represent the velocity in both the feature and the configuration space as:

$$\Delta r^{(t)} = \frac{r^{(t+\frac{\Delta t}{2})} - r^{(t-\frac{\Delta t}{2})}}{\Delta t/C_{fr}}, \quad (15)$$

$$\Delta s(I^{(t)}) = \frac{s(I^{(t+\frac{\Delta t}{2})}) - s(I^{(t-\frac{\Delta t}{2})})}{\Delta t/C_{fr}}, \quad (16)$$

where  $C_{fr}$  is the frame rate of the captured video.

However, sampling by a fixed time step ( $\Delta t$ ) leads to a limited number of samples ( $N_I - \Delta t$ ) and can result in over-fitting. To overcome this issue, we break the sequential order of the time index to generate more training data from  $I^{(t)}$  and  $r^{(t)}$ . In particular, we assume the manipulation task can be observed as a Markov process [65] and each step is independent from every other. In this case, the sampling rates are given as follows, (when the total sampling amount is  $n$ ):

$$\Delta r^{(t)} = \frac{r^{(l_t)} - r^{(l_{t+n})}}{(l_t - l_{t+n})/C_{fr}}, \quad (17)$$

$$\Delta s(I^{(t)}) = \frac{s(I^{(l_t)}) - s(I^{(l_{t+n})})}{(l_t - l_{t+n})/C_{fr}}, \quad (18)$$

where  $l_{1, \dots, 2n}$  is a set of indices randomly generated, and  $l_t \in [1, \dots, N_I]$ . In order to build a more concise dictionary, we also apply K-Means Clustering [66] on the feature space, which enhance the performance and prevent the over-fitting problem.

In practice, the visual feedback dictionary can be regarded as an approximation of the interaction function  $H$  in Equation 6). The overall algorithm to compute the dictionary is given in Algorithm 2.

2) *Sparse representation:* At runtime, we use sparse linear representation [67] to compute the velocity of the controller from the visual feedback dictionary. These representations tend to assign zero weights to most irrelevant or redundant features and are used to find a small subset of most predictive features in the high dimensional feature space. Given a noisy observation of a feature at runtime ( $s$ ) and the visual feedback dictionary constructed by features  $\{\Delta s^{(i)}\}$  with labels  $\{\Delta r^{(i)}\}$ , we represent  $\Delta s$  by  $\hat{\Delta s}$ , which is a sparse linear combination of  $\{\Delta s^{(i)}\}$ , where  $\beta$  is the sparsity-inducing  $L_1$  term. To deal with noisy data, we rather use the  $L_2$  norm on the data-fitting term and formulate the resulting sparse representation as:

$$\hat{\beta} = \underset{\beta}{\operatorname{argmin}} \left( \|\min(\Delta s - \sum_i \beta_i \Delta s^{(i)})\|_2^2 + \alpha \|\beta\|_1 \right), \quad (19)$$

where  $\alpha$  is a slack variable that is used to balance the trade-off between fitting the data perfectly and using a sparse solution. The sparse coefficient  $\beta^*$  is computed using a

---

**Algorithm 2** Building the visual feedback dictionary

---

**Input:** image stream  $\{I^{(t)}\}$  and positions of end-effectors  $\{\mathbf{r}^{(t)}\}$  with sampling amount  $n$ , dictionary size  $N_{dic}$   
**Output:** Visual feedback dictionary  $\{\{\Delta\mathbf{s}_d^{(i)}\}, \{\Delta\mathbf{r}_d^{(i)}\}\}$

- 1:  $\{\Delta\mathbf{s}_d\} = \{\}, \{\Delta\mathbf{r}_d\} = \{\}$
- 2:  $\triangleright$  generate random indices for sampling
- 3:  $l = N_I \text{RAND}(2n)$
- 4: **for**  $i = 1, \dots, n$  **do**
- 5:    $\Delta\mathbf{s}^{(i)} = \mathbf{s}(I^{(l(i))}) - \mathbf{s}(I^{(l(i+n))})$   $\triangleright$  sampling
- 6:    $\Delta\mathbf{r}^{(i)} = \mathbf{r}^{(l(i))} - \mathbf{r}^{(l(i+n))}$   $\triangleright$  sampling
- 7: **end for**
- 8:  $\triangleright$  compute the centers of the feature set for clustering
- 9:  $\text{centers} = \text{K-MEANS}(\{\Delta\mathbf{s}^{(i)}\}, N_{dic})$
- 10: **for**  $i = 1, \dots, N_{dic}$  **do**
- 11:    $j = \text{argmin}_i \|\text{centers}[i] - \mathbf{s}^{(i)}\|$
- 12:    $\{\Delta\mathbf{s}_d\} = \{\Delta\mathbf{s}_d, \Delta\mathbf{s}^{(j)}\}$   $\{\Delta\mathbf{r}_d\} = \{\Delta\mathbf{r}_d, \Delta\mathbf{r}^{(j)}\}$
- 13: **end for**
- 14: **return**  $\{\Delta\mathbf{s}_d\}, \{\Delta\mathbf{r}_d\}$

---

minimization formulation:

$$\beta^* = \underset{\beta}{\text{argmin}} \left( \sum_i \rho(\Delta\mathbf{s}_i^* - \sum_j \beta_j \Delta\mathbf{s}_i^{(j)}) + \alpha \sum_j \|\beta_j\|_1 \right). \quad (20)$$

After  $\hat{\beta}$  is computed, the observation  $\Delta\hat{\mathbf{s}}$  and the probable label  $\Delta\hat{\mathbf{r}}$  can be reconstructed by the visual feedback dictionary:

$$\Delta\hat{\mathbf{s}} = \sum_i \hat{\beta}_i \Delta\mathbf{s}_i^{(i)} \quad \Delta\hat{\mathbf{r}} = \sum_i \hat{\beta}_i \Delta\mathbf{r}_i^{(i)} \quad (21)$$

The corresponding  $\Delta\mathbf{r}^*$  of the  $i$ -th DOF in the configuration is given as:

$$\Delta\mathbf{r}_i^* = \sum_j \beta_j^* \Delta\mathbf{r}_i^{(j)}, \quad (22)$$

where  $\Delta\mathbf{s}_i^{(j)}$  denotes the  $i$ -th datum of the  $j$ -th feature,  $\Delta\mathbf{s}_i^*$  denotes the value of the response, and the norm-1 regularizer  $\sum_j \|\beta_j\|_1$  typically results in a sparse solution in the feature space.

3) *Goal configuration and mapping:* We compute the goal configuration and the corresponding HOW-features based on the underlying manipulation task at runtime. Based on the configuration, we compute the velocity of the end-effector. The different ways to compute the goal configuration are:

- For the task of manipulating deformable objects to a single state  $c^*$ , the goal configuration can be represented simply by the visual feature of the desired state  $\mathbf{s}^* = \mathbf{s}(I^*)$ .
- For the task of manipulating deformable objects to a hidden state  $c^*$ , which can be represented by a set of states of the object  $c^* = \{c_1, \dots, c_n\}$  as a set of visual features  $\{\mathbf{s}(I_1), \dots, \mathbf{s}(I_n)\}$ . We modify the formulation in Equation 6 to compute  $\delta\mathbf{r}$  as:

$$\delta\mathbf{r} = \min_i H(\eta(\mathbf{s}(I) - \mathbf{s}(I_j))) \quad (23)$$

- For a complex task, which can be represented using a sequential set of states  $\{c_1, \dots, c_n\}$ , we estimate the sequential cost of each state as  $\text{cost}(c_i)$ . We use a modification that tends to compute the state with the lowest sequential cost:

$$i^* = \underset{i}{\text{argmin}} \left( \text{cost}(c_i) + H(\eta(\mathbf{s}(I) - \mathbf{s}(I_i))) \right). \quad (24)$$

After  $i^*$  is computed, the velocity for state  $c_i$  is determined by  $\mathbf{s}(I_{i^*})$ , and  $c_i$  is removed from the set of goals for subsequent computations.

## VI. CONTROLLER DESIGN: NONLINEAR GAUSSIAN PROCESS REGRESSION

### A. Interaction function learning

Unlike many previous methods assuming the interaction function  $H(\cdot)$  to be a linear function, here we consider  $H(\cdot)$  as a general and highly nonlinear function determining how the movement of the manipulated points is converted into the feature space. The learning of the function  $H$  requires a flexible and non-parametric method. Our solution is to use the Gaussian Process Regression (GPR) to fit the interaction function in an online manner.

GPR is a nonparametric regression technique which defines a distribution over functions and the inference takes place directly in the functional space given the covariance and mean of the functional distribution. For our manipulation problem, we formulate the interaction function  $H$  as a Gaussian process:

$$H \sim GP(m(\delta\mathbf{s}), k(\delta\mathbf{s}, \delta\mathbf{s}')) \quad (25)$$

where  $\delta\mathbf{s}$  still denotes the velocity in the feature space. For the covariance or kernel function  $k(\delta\mathbf{s}, \delta\mathbf{s}')$ , we are using the Radius Basis Function (RBF) kernel:  $k(\delta\mathbf{s}, \delta\mathbf{s}') = \exp\left(-\frac{\|\delta\mathbf{s} - \delta\mathbf{s}'\|^2}{2\sigma_{RBF}^2}\right)$ , where the parameter  $\sigma_{RBF}$  sets the spread of the kernel. For the mean function  $m(\delta\mathbf{s})$ , we are using the linear mean function  $m(\delta\mathbf{s}) = \mathbf{W}\delta\mathbf{s}$ ,  $\mathbf{W}$  is the linear regression weight matrix. We choose to use a linear mean function rather than the common zero mean function, because previous work [18] showed that the adaptive Jacobian method, which can be considered as a special version of our method using the linear mean function, is able to capture a large part of the interaction function  $H$ . As a result, a linear mean function can result in faster convergence of our online learning process and also provide a relatively accurate prediction in the unexplored region in the feature space. The matrix  $\mathbf{W}$  is learned online by minimizing a squared error  $Q = \frac{1}{2} \|\delta\mathbf{r} - \mathbf{W}\delta\mathbf{s}\|^2$  with respect to the weight matrix  $\mathbf{W}$ .

Given a set of training data in terms of pairs of feature space velocities and manipulated point velocities  $\{(\delta\mathbf{s}_t, \delta\mathbf{r}_t)\}_{t=1}^N$  during the previous manipulation process, the standard GPR computes the distribution of the interaction function as a Gaussian process  $H(\delta\mathbf{s}) \sim \mathcal{N}(\mu(\delta\mathbf{s}), \sigma^2(\delta\mathbf{s}))$ , where GP's mean function is

$$\begin{aligned} \mu(\delta\mathbf{s}) = m(\delta\mathbf{s}) + \mathbf{k}^T(\delta\mathbf{S}, \delta\mathbf{s}) \cdot [\mathbf{K}(\delta\mathbf{S}, \delta\mathbf{S}) + \sigma_n^2 \mathbf{I}]^{-1} \\ \cdot (\delta\mathbf{R} - m(\delta\mathbf{S})) \end{aligned} \quad (26)$$

and GP's covariance function is

$$\begin{aligned}\sigma^2(\delta\mathbf{s}) &= k(\delta\mathbf{s}, \delta\mathbf{s}) - \mathbf{k}^T(\delta\mathbf{s}, \delta\mathbf{s}) \cdot [\mathbf{K}(\delta\mathbf{s}, \delta\mathbf{s}) + \sigma_n^2 \mathbf{I}]^{-1} \\ &\quad \cdot \mathbf{k}(\delta\mathbf{s}, \delta\mathbf{s}).\end{aligned}\quad (27)$$

Here  $\delta\mathbf{S}$  and  $\delta\mathbf{R}$  are matrices corresponding to the stack of  $\{\delta\mathbf{s}_t\}_{t=1}^N$  and  $\{\delta\mathbf{r}_t\}_{t=1}^N$  in the training data, respectively.  $\mathbf{K}$  and  $\mathbf{k}$  are matrices and vectors computed using a given covariance function  $k(\cdot, \cdot)$ . The matrix  $\mathbf{A} = \mathbf{K} + \sigma_n^2 \mathbf{I}$  is called the Gram matrix, and the parameter  $\sigma_n$  estimates the uncertainty or noise level of the training data.

### B. Real-time online GPR

In the deformation object manipulation process, the data  $(\delta\mathbf{s}_t, \delta\mathbf{r}_t)$  is generated sequentially, and thus at each time step  $t$ , we need to update the GP interaction function  $H_t(\delta\mathbf{s}) \sim \mathcal{N}(\mu_t(\delta\mathbf{s}), \sigma^2(\delta\mathbf{s}))$  at an interactive manner, with

$$\begin{aligned}\mu_t(\delta\mathbf{s}) &= m(\delta\mathbf{s}) + \mathbf{k}^T(\delta\mathbf{s}_t, \delta\mathbf{s}) \cdot [\mathbf{K}(\delta\mathbf{s}_t, \delta\mathbf{s}_t) + \sigma_n^2 \mathbf{I}]^{-1} \\ &\quad \cdot (\delta\mathbf{R}_t - m(\delta\mathbf{S}_t))\end{aligned}\quad (28)$$

and

$$\begin{aligned}\sigma_t^2(\delta\mathbf{s}) &= k(\delta\mathbf{s}, \delta\mathbf{s}) - \mathbf{k}^T(\delta\mathbf{S}_t, \delta\mathbf{s}) \cdot [\mathbf{K}(\delta\mathbf{S}_t, \delta\mathbf{S}_t) + \sigma_n^2 \mathbf{I}]^{-1} \\ &\quad \cdot \mathbf{k}(\delta\mathbf{S}_t, \delta\mathbf{s}).\end{aligned}\quad (29)$$

In the online GPR, we need to perform the inversion of the Gram matrix  $\mathbf{A}_t = \mathbf{K}(\delta\mathbf{S}_t, \delta\mathbf{S}_t) + \sigma_n^2 \mathbf{I}$  repeatedly with a time complexity  $\mathcal{O}(N^3)$ , where  $N$  is the size of the current training set involved in the regression. Such cubic complexity makes the training process slow for long manipulation sequence where the training data size  $N$  increases quickly. In addition, the growing up of the GP model will reduce the newest data's impact on the regression result and make the GP fail to capture the change of the objects's deformation parameters during the manipulation. This is critical for deformable object manipulation, because the interaction function  $H$  is derived from the local force equilibrium and thus is only accurate in a small region.

Motivated by previous work about efficient offline GPR [68]–[71], we here present a novel online GPR method called the *Fast Online GPR* (FO-GPR) to reduce the high computational cost and to adapt to the changing deformation properties while updating the deformation model during the manipulation process. The main idea of FO-GPR includes two parts: 1) maintaining the inversion of the Gram matrix  $\mathbf{A}_t$  incrementally rather using direct matrix inversion; 2) restricting the size of  $\mathbf{A}_t$  to be smaller than a given size  $M$ , and  $\mathbf{A}_t$ 's size exceeds that limit, using a selective “forgetting” method to replace stale or uninformative data by the fresh new data point.

1) *Incremental update of Gram matrix  $\mathbf{A}_t$ :* Suppose at time  $t$ , the size of  $\mathbf{A}_t$  is still smaller than the limit  $M$ . In this case,  $\mathbf{A}_t$  and  $\mathbf{A}_{t-1}$  are related by

$$\mathbf{A}_t = \begin{bmatrix} \mathbf{A}_{t-1} & \mathbf{b} \\ \mathbf{b}^T & c \end{bmatrix}, \quad (30)$$

where  $\mathbf{b} = \mathbf{k}(\delta\mathbf{S}_{t-1}, \delta\mathbf{s}_t)$  and  $c = k(\delta\mathbf{s}_t, \delta\mathbf{s}_t) + \sigma_n^2$ . According to the HelmertWolf blocking inverse property, we can compute the inverse of  $\mathbf{A}_t$  based on the inverse of  $\mathbf{A}_{t-1}$ :

$$\begin{aligned}\mathbf{A}_t^{-1} &= \begin{bmatrix} \left(\mathbf{A}_{t-1} - \frac{1}{c}\mathbf{b}\mathbf{b}^T\right)^{-1} & -\frac{1}{r}\mathbf{A}_{t-1}^{-1}\mathbf{b} \\ -\frac{1}{r}\mathbf{b}^T\mathbf{A}_{t-1}^{-1} & \frac{1}{r} \end{bmatrix} \\ &= \begin{bmatrix} \mathbf{A}_{t-1}^{-1} + \frac{1}{r}\mathbf{A}_{t-1}^{-1}\mathbf{b}\mathbf{b}^T\mathbf{A}_{t-1}^{-1} & -\frac{1}{r}\mathbf{A}_{t-1}^{-1}\mathbf{b} \\ -\frac{1}{r}\mathbf{b}^T\mathbf{A}_{t-1}^{-1} & \frac{1}{r} \end{bmatrix},\end{aligned}\quad (31)$$

where  $r = c - \mathbf{b}^T\mathbf{A}_{t-1}^{-1}\mathbf{b}$ . In this way, we achieve the incremental update of the inverse Gram matrix from  $\mathbf{A}_{t-1}^{-1}$  to  $\mathbf{A}_t^{-1}$ , and the computational cost is  $\mathcal{O}(N^2)$  rather than  $\mathcal{O}(N^3)$  of direct matrix inversion. This acceleration enables fast GP model update during the manipulation process.

2) *Selective forgetting in online GPR:* When the size of  $\mathbf{A}_{t-1}$  reaches the limit  $M$ , we use a “forgetting” strategy to replace the most uninformative data by the fresh data points while keeping the size of  $\mathbf{A}_t$  to be  $M$ . In particular, we choose to forget the  $i_*$  data point that is the most similar to other data points in terms of the covariance, i.e.,

$$i_* = \operatorname{argmax}_i \sum_j \mathbf{A}[i, j], \quad (32)$$

where  $\mathbf{A}[i, j]$  denotes the covariance value stored in the  $i$ -th row and  $j$ -th column in  $\mathbf{A}$ , i.e.,  $k(\delta\mathbf{s}_i, \delta\mathbf{s}_j) + \sigma_n^2$ .

Given the new data  $(\delta\mathbf{s}_t, \delta\mathbf{r}_t)$ , we need to update  $\delta\mathbf{S}_t$ ,  $\delta\mathbf{R}_t$ , and  $\mathbf{A}_t^{-1} = [\mathbf{K}(\delta\mathbf{S}_t, \delta\mathbf{S}_t) + \sigma_n^2 \mathbf{I}]^{-1}$  in Equation 28 and 29 by swapping data terms related to  $\delta\mathbf{s}_t$  and  $\delta\mathbf{s}_{i_*}$ , in order to update the interaction function  $H_t$ .

The incremental update for  $\delta\mathbf{S}_t$  and  $\delta\mathbf{R}_t$  is trivial:  $\delta\mathbf{S}_t$  is identical to  $\delta\mathbf{S}_{t-1}$  except  $\delta\mathbf{S}_t[i_*]$  is  $\delta\mathbf{s}_t$  rather than  $\delta\mathbf{s}_{i_*}$ ;  $\delta\mathbf{R}_t$  is identical to  $\delta\mathbf{R}_{t-1}$  except  $\delta\mathbf{R}_t[i_*]$  is  $\delta\mathbf{r}_t$  rather than  $\delta\mathbf{r}_{i_*}$ .

We then discuss how to update  $\mathbf{A}_t$  from  $\mathbf{A}_{t-1}$ . Since  $\mathbf{A}_t - \mathbf{A}_{t-1}$  is only non-zero at the  $i_*$ -th column or the  $i_*$ -th row:

$$(\mathbf{A}_t - \mathbf{A}_{t-1})[i, j] = \begin{cases} 0, & i, j \neq i_* \\ k(\delta\mathbf{s}_i, \delta\mathbf{s}) - k(\delta\mathbf{s}_i, \delta\mathbf{s}_{i_*}), & j = i_* \\ k(\delta\mathbf{s}_j, \delta\mathbf{s}) - k(\delta\mathbf{s}_j, \delta\mathbf{s}_{i_*}), & i = i_* \end{cases}$$

this matrix can be written as the multiplication of two matrices  $\mathbf{U}$  and  $\mathbf{V}$ , i.e.,  $\mathbf{A}_t - \mathbf{A}_{t-1} = \mathbf{U}\mathbf{V}^T$ , where

$$\mathbf{U} = [\mathbf{e}_{i_*} \quad (\mathbf{I} - \frac{1}{2}\mathbf{e}_{i_*}\mathbf{e}_{i_*}^T)(\mathbf{k}_t - \mathbf{k}_{t-1})]$$

and

$$\mathbf{V} = [(\mathbf{I} - \frac{1}{2}\mathbf{e}_{i_*}\mathbf{e}_{i_*}^T)(\mathbf{k}_t - \mathbf{k}_{t-1}) \quad \mathbf{e}_{i_*}].$$

Here  $\mathbf{e}_{i_*}$  is a vector that is all zero but one at the  $i_*$ -th item,  $\mathbf{k}_t$  is the vector  $\mathbf{k}(\delta\mathbf{S}_t, \delta\mathbf{s}_t)$  and  $\mathbf{k}_{t-1}$  is the vector  $\mathbf{k}(\delta\mathbf{S}_{t-1}, \delta\mathbf{s}_{i_*})$ . Both  $\mathbf{U}$  and  $\mathbf{V}$  are size  $M \times 2$  matrices.

Then using Sherman-Morrison formula, there is

$$\begin{aligned}\mathbf{A}_t^{-1} &= (\mathbf{A}_{t-1} + \mathbf{U}\mathbf{V}^T)^{-1} \\ &= \mathbf{A}_{t-1}^{-1} - \mathbf{A}_{t-1}^{-1}\mathbf{U}(\mathbf{I} + \mathbf{V}^T\mathbf{A}_{t-1}^{-1}\mathbf{U})^{-1}\mathbf{V}^T\mathbf{A}_{t-1}^{-1},\end{aligned}\quad (33)$$

which provides the incremental update scheme for the Gram matrix  $\mathbf{A}_t$ . Since  $\mathbf{I} + \mathbf{V}^T\mathbf{A}_{t-1}^{-1}\mathbf{U}$  is a  $2 \times 2$  matrix, its inversion can be computed in  $\mathcal{O}(1)$  time. Therefore, the

incremental update computation is dominated by the matrix-vector multiplication and thus the time complexity is  $\mathcal{O}(M^2)$  rather than  $\mathcal{O}(M^3)$ .

A complete description for FO-GPR is as shown in Algorithm 3.

---

**Algorithm 3** FO-GPR

---

**Input:**  $\delta\mathbf{S}_{t-1}, \delta\mathbf{R}_{t-1}, \mathbf{A}_{t-1}, \delta\mathbf{s}_t, \delta\mathbf{r}_t$   
**Output:**  $\delta\mathbf{S}_t, \delta\mathbf{R}_t, \mathbf{A}_t^{-1}$

- 1: **if**  $\dim(\mathbf{A}_{t-1}) < M$  **then**
- 2:    $\delta\mathbf{S}_t = [\delta\mathbf{S}_{t-1}, \delta\mathbf{s}_t]$
- 3:    $\delta\mathbf{R}_t = [\delta\mathbf{R}_{t-1}, \delta\mathbf{r}_t]$
- 4:    $\mathbf{A}_t^{-1}$  computed using Equation 31
- 5: **else**
- 6:    $i_*$  computed using Equation 32
- 7:    $\delta\mathbf{S}_t = \delta\mathbf{S}_{t-1}, \delta\mathbf{S}_t[i_*] = \delta\mathbf{s}_t$
- 8:    $\delta\mathbf{R}_t = \delta\mathbf{R}_{t-1}^m, \delta\mathbf{R}_t[i_*] = \delta\mathbf{r}_t$
- 9:    $\mathbf{A}_t^{-1}$  computed using Equation 33
- 10: **end if**

---

### C. Exploitation and exploration

Given the interaction function  $H_t$  learned by FO-GPR, the controller system predicts the required velocity to be executed by the end-effectors based on the error between the current state and the goal state in the feature space:

$$\delta\mathbf{r} = H_t(\gamma \cdot (\mathbf{s}^* - \mathbf{s})), \quad (34)$$

where  $\gamma$  is a scale factor as the feedback gain.

However, when there is no sufficient data, GPR cannot output control policy with high confidence, which typically happens in the early step of the manipulation or when the robot manipulates the object into a new unexplored configuration. Fortunately, the GPR framework provides a natural way to trade-off exploitation and exploration by sampling the control velocity from distribution of  $H_t$ :

$$\delta\mathbf{r} \sim \mathcal{N}(\mu_t, \sigma_t^2) \quad (35)$$

If  $\mathbf{s}_t$  is now in unexplored region with large  $\sigma_t^2$ , the controller will perform exploration around  $\mu_t$ ; if  $\mathbf{s}_t$  is in a well-explored region with small  $\sigma_t^2$ , the controller will output velocity close to  $\mu_t$ .

A complete description of the controller based on FO-GPR is shown in Figure 7.

### D. Convergence and stability analysis

We can prove that given more and more data, our GPR-based online learning converges to the true underlying deformation distribution and the resulting controller is stable.

The GPR prediction in Equation 26 and 34 includes two terms: The first term  $m(\delta\mathbf{s})$  actually corresponds to the adaptive Jacobian in [18] which has proven to be bounded and is able to asymptotically minimize the error between the current and the target states. The second term corresponds to a function  $H$  minimizing the functional

$$J[H] = \frac{1}{2} \|H\|_{RKHS}^2 + \frac{1}{2\sigma_n^2} \sum_{t=1}^N (\delta\mathbf{R}_t - H(\delta\mathbf{s}_t))^2, \quad (36)$$

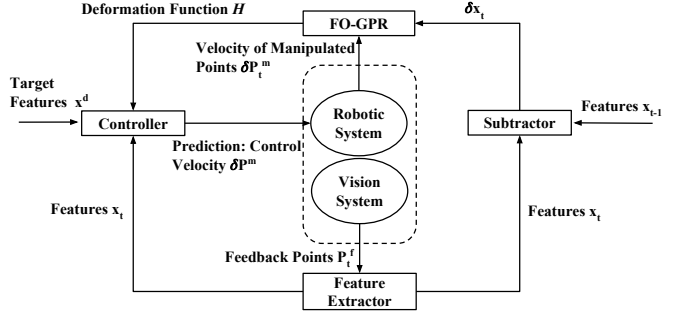


Fig. 7: An overview of our nonlinear DOM controller based on Gaussian Process Regression.

where  $\|H\|_{RKHS}$  is the RKHS (reproducing kernel Hilbert space) norm w.r.t the kernel  $k$ . According to [72], we can prove that this second term converges:

*Proposition 1:* The prediction function  $H$  converges to a true underlying interaction function  $\eta$ .

*Proof:* Let  $\mu(\delta\mathbf{S}, \delta\mathbf{R})$  be the probability measure from which the data pairs  $(\delta\mathbf{s}_t, \delta\mathbf{S}_t)$  are generated. We have

$$\mathbb{E}[\sum_{t=1}^N (\delta\mathbf{R}_t - H(\delta\mathbf{s}_t))^2] = N \int (\delta\mathbf{R} - H(\delta\mathbf{S}))^2 d\mu.$$

Let  $\eta(\delta\mathbf{S}) = \mathbb{E}[\delta\mathbf{R}|\delta\mathbf{S}]$  and  $\lambda_i$  be the  $i$ -th eigenfunction of the kernel function  $k$ , the  $J[H]$  functional becomes

$$J[H] = \frac{N}{2\sigma_n^2} \sum_{t=1}^{\infty} (\eta_t - H_t)^2 + \frac{1}{2} \sum_{t=1}^{\infty} \frac{H_t^2}{\lambda_t} \quad (37)$$

and its solution can then be computed as

$$H_t = \frac{\lambda_t}{\lambda_t + \sigma_n^2/N} \eta_t. \quad (38)$$

When  $n \rightarrow \infty$ ,  $\sigma_n^2/N \rightarrow 0$  and thus  $H$  converges to  $\eta$ . ■

After showing the convergence of Equation 26 and 34, we can perform local linearization for the nonlinear GPR prediction function and then design a Lyapunov function similar to [18] to show the stability of the GPR-based visual-servoing controller.

## VII. CONTROLLER DESIGN: RANDOM FOREST CONTROLLER

The GPR controller proposed above has two main limitations. First, the controller must be in the form of a mathematical function, and thus is not able to model more complicated controller required while dealing with large deformations. Second, the feature extraction step and control design step are independent.

Here, we present a another controller for DOM tasks. This controller uses random-forest [73] to model the mapping between the visual features of the object to an optimal control action of the manipulator. The topological structure of this random-forest-based controller is determined automatically based on the training data consisting of visual features and control actions. This enables us to integrate the overall process of training data classification and controller optimization

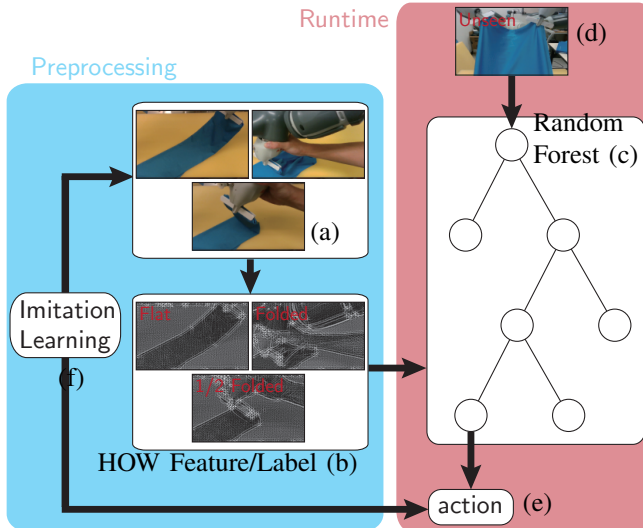


Fig. 8: The pipeline of learning a random forest-based DOM-controller that maps the visual feature (RGB-D image) to the control action. Given a sampled dataset (a), we first label each data point (shown as red text in (b)) to get a labeled dataset, (b). We then construct a random forest to classify the images, (c). After training, the random forest is used as a controller. Given an unseen visual observation (d), the observation is brought through the random forest to a set of leaf nodes. The optimal control actions are defined on these leaf nodes, (e). The entire process of labeling, classification, and controller optimization can be integrated into an imitation learning algorithm, (f).

into an imitation learning (IL) algorithm. Our approach enables joint feature extraction and controller optimization for DOM tasks.

The pipeline of our approach is illustrated in Figure 8 and it consists of two components. For preprocessing (the blue block), a dataset of object observations is labeled and features are extracted for each observation. This dataset is used to train our controller. During runtime (the red block), our algorithm takes the current  $\mathcal{O}(c)$  as input and generates the optimal action  $\mathbf{r}^* = \pi(\mathcal{O}(c)|\beta)$ , where  $\pi$  is the control policy and  $\beta$  is the controller's learnable parameter.

#### A. Random forest-based controller formulation

Our key contribution is a novel parametrization of  $\pi$  with the use of a random forest [73]. A random forest is an ensemble of  $K$  decision trees, where the  $k$ -th tree classifies  $\mathcal{O}(c)$  by bringing it to a leaf-node  $l_k(\mathcal{O}(c))$ , where  $1 \leq l_k(\mathcal{O}(c)) \leq L_k$  and  $L_k$  is the number of leaf-nodes in the  $k$ -th decision tree. The random forest makes its decision by bringing  $\mathcal{O}(c)$  through every tree and take the average. In order to use an already constructed random forest as a controller, we define an optimal control action  $r_{l,k}^*$  so that the final action is determined by averaging:

$$\mathbf{r}^* = \pi(\mathcal{O}(c)|\alpha, \beta) = \frac{1}{K} \mathbf{r}_{l_k(\mathcal{O}(c)), k}^*, \quad (39)$$

where we introduce an additional parameter  $\alpha$  that encodes the random forest's topology. As a result, the number of optimizable controller parameters is  $|\theta| = |\mathbf{r}^*| \sum_{k=1}^K L_k$ .

Such an extension to a random forest has two benefits. First, even if two decision trees give the same classification for an observation  $\mathcal{O}(c)$ , i.e., the class label of  $l_a(\mathcal{O}(c))$  equals that of  $l_b(\mathcal{O}(c))$ , we still assign separate optimal control actions,  $\mathbf{r}_{l_a,a}$  and  $\mathbf{r}_{l_b,b}$ , for optimization. This makes the controller more robust to bad predictions. Second, the number of optimized parameters is related to the random forest's topology. This reveals strong connection between feature extraction and controller parametrization. By automatically segmenting the state space into pieces (leaf-nodes) where different control actions need to be taken, fewer design decisions on the controller's side are exposed to the end-user. This makes our method less sensitive to parameters.

#### B. Controller optimization problem

Our controller training problem can take different forms depending on the available information about  $c^*$ . If  $\mathcal{O}(c^*)$  is known, then we can define a reward function:  $R(c) = \text{dist}(\mathcal{O}(c), \mathcal{O}(c^*))$ , where  $\text{dist}$  can be any distance measure between RGB-D images. In this setting, we want to solve the following reinforcement learning (RL) problem:

$$\underset{\alpha, \beta}{\text{argmax}} \mathbf{E}_{\tau \sim \pi} \left[ \sum_i^{\infty} \gamma^i R(c_i) \right], \quad (40)$$

where  $\tau = (c_1, c_2, \dots, c_\infty)$  is a trajectory sampled according to  $\pi$  and  $\gamma$  is the discount factor. Another widely used setting assumes  $\mathcal{O}(c^*)$  is unknown, but an expert is available to provide optimal control action  $\pi^*(\mathcal{O}(c))$ . In this case, we want to solve the following IL problem:

$$\underset{\alpha, \beta}{\text{argmax}} \mathbf{E}_{\tau \sim \pi} \left[ \sum_i^{\infty} \gamma^i \text{dist}(\pi^*(\mathcal{O}(c_i)), \pi(\mathcal{O}(c_i))) \right]. \quad (41)$$

Our method is designed for this IL problem and we assume that  $\mathcal{O}(c^*)$  is known even in an IL setting. This is because  $\mathcal{O}(c^*)$  is needed to construct the random forest. This assumption always holds when we are training in a simulated environment. We describe the method to perform these optimizations in Section VII-C.

#### C. Learning random forest-based controller

To find the controller parameters, we use an IL algorithm [54], which can be decomposed into two substeps: dataset sampling and controller optimization. The first step samples a dataset  $\mathcal{D} = \{\langle \mathcal{O}(c), \mathbf{r}^* \rangle\}$ , where each sample is a combination of cloth observation and optimal action. Our goal is to optimize the random forest-based controller with respect to  $\alpha, \beta$ , given  $\mathcal{D}$ .

1) *Random forest construction:* We first solve for  $\alpha$ , the topology of the random forest. Unfortunately, a random forest construction requires a labeled dataset that classifies the samples into a discrete set of classes. To generate these labels, we run a mean-shift clustering computation on the optimal actions,  $\mathbf{r}^*$ . In addition, we reduce the dimension of RGB-D image by extracting the HOW-feature (Section V).

After feature mapping, we get a modified dataset  $\bar{\mathcal{D}} = \{\langle \mathcal{F}(\mathcal{O}(c)), \mathcal{L}(\mathbf{r}^*) \rangle\}$ , where  $\mathcal{F}$  is the feature extractor such

that the extracted feature  $s = \mathcal{F}(\mathcal{O}(c))$  and  $\mathcal{L}$  is the mean-shift labeling.

To construct the random forest, we use a strategy that is similar to [74]. We construct  $K$  binary decision trees in a top-down manner, each using a random subset of  $\bar{\mathcal{D}}$ . Specifically, for each node of a tree, a set of random partitions is computed and the one with the maximal Shannon information gain [73] is adopted. Each tree is grown until a maximum depth is reached or the best Shannon information gain is lower than a threshold.

2) *Controller optimization*: After constructing the random forest, we define optimal control actions on each leaf-node of each decision tree and the optimal control action can be derived according to Equation 39. We can then optimize for  $\beta$ , i.e., all the  $\mathbf{r}_{l,k}^*$ , by solving the following optimization problem:

$$\operatorname{argmin}_{\mathbf{r}_{l,k}^*} \sum_{\langle \mathcal{O}(c), \mathbf{r}^* \rangle} \left\| \mathbf{r}^* - \frac{1}{K} \mathbf{r}_{l_k(\mathcal{O}(c)),k}^* \right\|^2. \quad (42)$$

This is a quadratic energy function that can be solved in closed form. However, a drawback of this energy is that every decision tree contributes equally to the final optimal action, making it less robust to outliers. To resolve this problem, we introduce a more robust model by exploiting sparsity. We assume that each leaf-node has a confidence value denoted by  $\gamma_{l,k} \in [0.01, 1]$  and the final optimal action is found by weighted averaging:

$$\mathbf{r}^* = \pi(\mathcal{O}(c) | \alpha, \beta) = \frac{\sum \gamma_{l_k(\mathcal{O}(c)),k} \mathbf{r}_{l_k(\mathcal{O}(c)),k}^*}{\sum \gamma_{l_k(\mathcal{O}(c)),k}}, \quad (43)$$

where a lower bound (0.01) on  $\gamma$  is used to avoid division-by-zero. Our final controller optimization takes the following form:

$$\begin{aligned} & \operatorname{argmin}_{\mathbf{r}_{l,k}^*, \gamma_{l,k}} \sum_{\langle \mathcal{O}(c), \mathbf{r}^* \rangle} \left\| \mathbf{r}^* - \frac{\sum \gamma_{l_k(\mathcal{O}(c)),k} \mathbf{r}_{l_k(\mathcal{O}(c)),k}^*}{\sum \gamma_{l_k(\mathcal{O}(c)),k}} \right\|^2 + \theta \|\gamma\|_1 \\ & \text{s.t. } \gamma_{l,k} \in [0.01, 1], \end{aligned} \quad (44)$$

which can be solved using an L-BFGS-B optimizer [75]. Finally, both the random forest construction and the controller optimization are integrated into the IL algorithm as outlined in Algorithm 4.

3) *Analysis*: In typical DOM applications, data are collected using numerical simulations. Unfortunately, the high dimensionality of  $c$  induces a high computational cost of simulations and generating a large dataset can be quite difficult. Therefore, we design our method so that it can be used with small datasets. Our method's performance relies on two parameters: the random forest's stopping criterion (i.e., the threshold of gain in Shannon entropy) and the L1-sparsity of leaf-node confidences,  $\theta$ . We choose to use a large shannon entropy threshold so that the random forest construction stops early, leaving us with a relatively small of leaf-nodes, so that  $|\beta|$  is small. We also fix  $\theta$  as a very small constant.

We expect that, with a large enough number of IL iterations, both the number of nodes in each decision tree of

**Algorithm 4** Training DOM-controller using imitation learning algorithm.

---

**Input:** Initial guess of  $\alpha, \beta$ , optimal policy  $\pi^*$   
**Output:** Optimized  $\alpha, \beta$

- 1:  $\triangleright$  IL outer loop
- 2: **while** IL has not converged **do**
- 3:      $\triangleright$  Generate training data based on current controller
- 4:     Sample  $\mathcal{D}$  by querying  $\pi^*$  as in [54]
- 5:      $\triangleright$  Label each data sample by mean-shift
- 6:     Run mean-shift on  $\{\mathbf{r}^*\}$  to get  $\mathcal{L}$
- 7:      $\triangleright$  Extract HOW feature for each data sample
- 8:     **for** each  $\mathcal{O}(c)$  **do**
- 9:         Extract HOW feature  $\mathcal{F}(\mathcal{O}(c))$  as in Section IV
- 10:     **end for**
- 11:     Define  $\bar{\mathcal{D}} = \{\langle \mathcal{F}(\mathcal{O}(c)), \mathcal{L}(\mathbf{r}^*) \rangle\}$
- 12:      $\triangleright$  Construct random forest, i.e.,  $\alpha$
- 13:     **for**  $1 \leq k \leq K$  **do**
- 14:         Sample random subset of  $\bar{\mathcal{D}}$
- 15:         Construct  $k$ -th binary decision tree using [74]
- 16:     **end for**
- 17:      $\triangleright$  Learn a new controller, i.e., determine  $\beta$
- 18:     Solve Equation 44 using L-BFGS-B [75]
- 19: **end while**

---

the random forest ( $\alpha$ ) and the optimal actions on the leaf-nodes ( $\beta$ ) will converge. Indeed, such convergence can be guaranteed by the following Lemma.

*Lemma 7.1: When the number of IL iterations  $N \rightarrow \infty$ , the distribution incurred by the random forest-based controller will converge to a stationary distribution and the expected classification error of random forest will converge to zero.*

*proof:* Assuming that Algorithm 4 generates a controller  $\pi^n$  at the  $n$ -th iteration, Lemma 4.1 of [54] showed that  $\pi^n$  incurs a distribution that converges when  $n \rightarrow \infty$ . Obviously, the number of data samples used to train the random forest also increases to  $\infty$  with  $n \rightarrow \infty$ . The expected error of random forest's classification on a stationary distribution converges to zero according to Theorem 5 of [76].

In Section VIII-C, we will further show that, empirically, the number of leaf-nodes in the random forest also converges.

## VIII. EXPERIMENTS AND RESULTS

We evaluate our proposed DOM framework using one dual-arm robot (ABB Yumi) with 7 degrees-of-freedom in each arm. To get precise information of the 3D object to be manipulated, we set up a vision system including two 3D cameras with different perception fields and precision: one realsense SR300 camera for small objects and one ZR300 camera for large objects. We compute the Cartesian coordinates of the end-effectors of the ABB YuMi as the controlling configuration  $r \in \mathbb{R}^6$  and use an inverse kinematics-based motion planner [77] directly. The entire manipulation system is shown in Figure 1.

### A. Deformable object manipulation using HOW features

To evaluate the effectiveness of combining the HOW feature with the basic visual servoing manipulation controller, we use 6 benchmarks (as shown in Figure 9) with different clothes, which have different material characteristics and shapes. Moreover, we use different initial and goal states depending on the task, e.g. stretching or folding. The details are listed in Table II. In these tasks, we use three different forms of goal configurations for the deformable object manipulations, as discussed in Section V-B.3.

For benchmarks 1-3, the task is to manipulate the cloth with human participation. The human is assisted with the task, but the task also introduces external perturbations. Our approach makes no assumptions about the human motion, and only uses the visual feedback to guess the human's behavior. In benchmark 1, the robot must anticipate the human's pace and forces for grasping to fold the towel in the air. In benchmark 2, the robot needs to process a complex task with several goal configurations when performing a folding task. In benchmark 3, the robot is asked to follow the human's actions to maintain the shape of the sheet. For benchmarks 4-6, the task corresponds to manipulating the cloth without human participation and we specify the goal configurations. All 6 benchmarks are defined with goal states/features of the cloth, regardless of whether if there is a human moving the cloth or not. Because different states the cloth can be precisely represented and corresponding controlling parameters can be computed, the robot can perform complicated tasks as well.

1) *Benefits of HOW features:* There are many standard techniques to compute low-dimensional features of deformable models from RGB data known in computer vision and image processing. These include standard HOG and color histograms. We evaluated the performance of HOW-features along with the others and also explore the combination of these features. The test involves measuring the success rate of the manipulator in moving towards the goal configuration based on the computed velocity, as given by Equation 8. We obtain best results in our benchmarks using HOG+HOW features. The HOG features capture the edges in the image and the HOW captures the wrinkles and deformation, so their combination works well. For benchmarks 1 and 2, the shapes of the objects changes significantly and HOW can easily capture the deformation by enhancing the edges. For benchmarks 3, 4, and 5, HOW can capture the deformation by the shadowed area of wrinkles. For benchmark 6, the total shadowed area continuously changes through the process, in which the color histogram describes the feature slightly better.

2) *Benefits of sparse representation:* The main parameter related to the visual feedback dictionary that governs the performance is its size. At runtime, it is also related to the choice of the slack variable in the sparse representation. As the size of the visual feedback dictionary grows, the velocity error tends to reduce. However, after reaching a certain size, the dictionary contributes less to the control policy mapping.

That implies that there is redundancy in the visual feedback dictionary.

The performance of sparse representation computation at runtime is governed by the slack variable  $\alpha$  in Equations 19 and 20. This parameter provides a tradeoff between data fitting and sparse solution and governs the velocity error  $\|\delta\mathbf{r} - \delta\mathbf{r}^*\|_2$  between the desired velocity  $\delta\mathbf{r}^*$  and the actual velocity  $\delta\mathbf{r}$ . In practice,  $\alpha$  affects the convergence speed. If  $\alpha$  is small, the sparse computation has little or no impact and the solution tends to a common linear regression. If  $\alpha$  is large, then we suffer from over-fitting.

### B. Nonlinear DOM controller based on GPR

For FO-GPR parameters, we set the observation noise  $\sigma_n = 0.001$ , the RBF spread width  $\sigma_{RBF} = 0.6$ , the maximum size of the Gram matrix  $M = 300$  and  $m(\delta\mathbf{s}) = 0$  when do comparison with Jacobian-based method. The executing rate of our approach is 30 FPS.

To evaluate the performance of the GPR-based nonlinear DOM controller, we design different manipulation tasks involving distinct objects as shown in Figure 11. In these tasks, the feedback points can either be all object points observed by the camera or several marked points (similar to what is done in [18]) critical for accomplishing a task.

- *Rolled towel bending:* This task aims at bending a rolled towel in to a specific goal shape as shown in Figure 11a. We use a 4-dimension feature vector  $\mathbf{s} = [\mathbf{c}, d]$  as the feature vector used in the FO-GPR driven visual-servo, where  $\mathbf{c}$  is the centroid feature described by Equation 10 and  $d$  is the distance feature as described by Equation 12 for two feature points on the towel.
- *Plastic sheet bending:* This goal of this task is to manipulate a plastic sheet into a preassigned curved status as shown in Figure 11b. We use a 4-dimension feature vector  $\mathbf{s} = [\mathbf{c}, \sigma]$  to describe the state of the plastic sheet, where  $\mathbf{c}$  is the centroid feature described by Equation 10 and  $\sigma$  is the surface variation feature computed by Equation 13. In Figure 11c, we also perform a task where the sheet is partially observed during the manipulation to demonstrate the robustness and stability of our proposed controller.
- *Peg-in-hole for fabrics:* This task aims at moving cloth pieces so that the pins can be inserted into the corresponding holes on the fabric. Two different types of fabric with different stiffness have been tested in our experiment: one is an unstretchable fabric as shown in Figure 11d and the other is a stretchable fabric as shown in Figure 11e. The 6-dimension feature vector  $\mathbf{s} = \rho$  is the position of feedback points as described in Equation 11.
- *Towel folding:* This task aims at flattening and folding a towel into a desired state as shown in Figure 11f. We use a binned histogram of extended FPFH, which generates a feature vector of 135 dimensions, to describe the towel's shape. Since the feature has a large dimension, for this experiment we need to manually move the robot in the beginning to explore sufficient data so that the

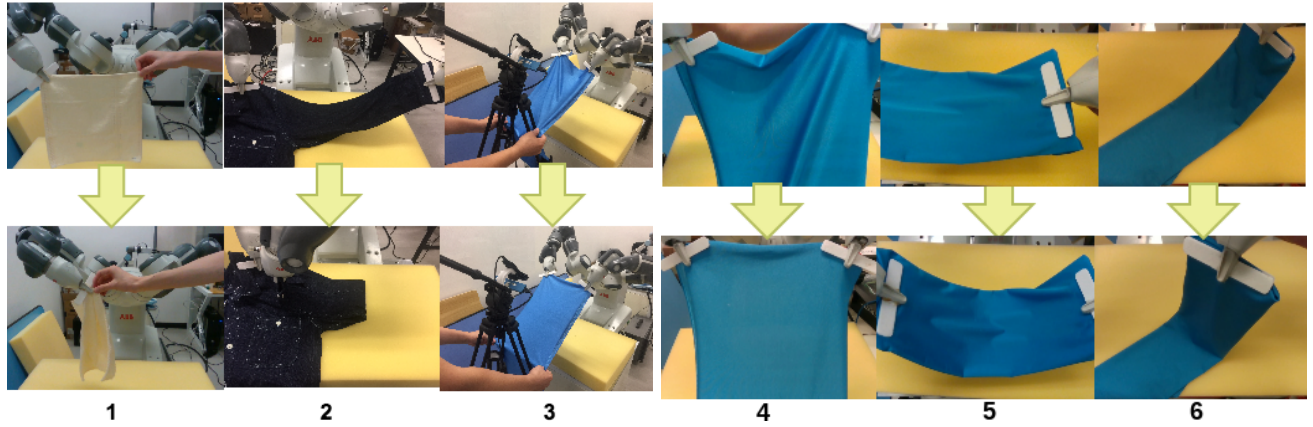


Fig. 9: We highlight the performance of using HOW features in DOM tasks on six benchmarks: (1) human-robot jointly folding a cloth with one hand each, (2) robot folding a cloth with two hands, (3) human-robot stretching a cloth with four combined hands, (4) flattening, (5) placement, (6) folding. The top row shows the initial state for each task and the bottom row is the final state. Our approach can handle the perturbations due to human movements.

Benchmark#	Object	Initial State	Task/Goal
1	towel	unfold in the air	fold with human
2	shirt	shape (set by human)	fixed shape
3	unstretchable cloth	position (set by human)	fixed shape
4	stretchable cloth	random	flattening
5	stretchable cloth	random	placement
6	stretchable cloth	unfolded shape on desk	folded shape

TABLE II: Benchmark tasks for accomplishing DOM tasks using HOW feature as the feedback: We highlight various complex manipulation tasks performed using our algorithm. Three of them involve human-robot collaboration and we demonstrate that our method can handle external forces and perturbations applied to the cloth. We use cloth benchmarks of different material characteristics. The initial state is a random configuration or an unfolded cloth on a table, and we specify the final configuration for the task. The benchmark numbers correspond to the numbers shown in Figure 9.

Feature	Benchmark 4	Benchmark 5	Benchmark 6
HOG	71.44%	67.31%	82.62%
Color Histograms	62.87%	53.67%	<b>97.04%</b>
HOW	92.21%	71.97%	85.57%
HOW+HOG	<b>94.53%</b>	<b>84.08%</b>	95.08%

TABLE III: Comparison between deformable object features: We evaluated the success rate of the manipulator based on different features in terms of reaching the goal configuration based on the velocity computed using those features. For each experiment, the number of goals equals the number of frames. There are 393, 204 and 330 frames in benchmarks 4, 5, and 6, respectively. Overall, we obtain the best performance by using HOG + HOW features.

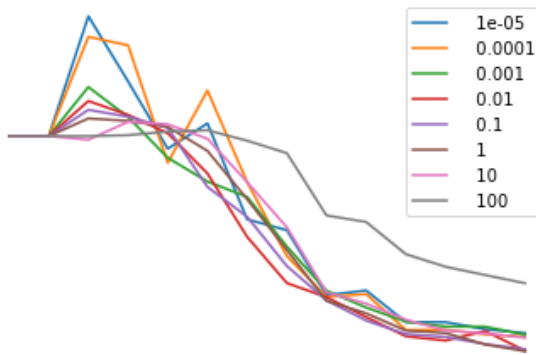


Fig. 10: Parameter selection for visual feedback dictionary and sparse representation: We vary the dictionary size on the  $x$ -axis and compute the velocity error for different values of  $\alpha$  chosen for sparse representation for benchmark 4.

FO-GPR can learn a good enough initial model for the complex deformation function.

Our FO-GPR based manipulation control is able to accomplish all the five tasks efficiently and accurately. The success rate is around 70% for the peg-in-hole task and 90% for other tasks.

Next, we provide some quantitative analysis of our approach by comparing with some state-of-the-art approaches.

1) *Comparison of computational cost with standard GPR:* As shown in Figure 12a, the time cost of the standard GPR operation in each iteration increases significantly when the number of training points increases, which makes the online deformation function update impossible. Our FO-GPR method's time cost is always under 2 ms. We also compare the time cost of each complete cycle of the manipulation process, including feature extraction, tracking, robot control, and GPR, and the result is shown in Figure 12b. Again, the time cost of manipulation using standard GPR fluctuates

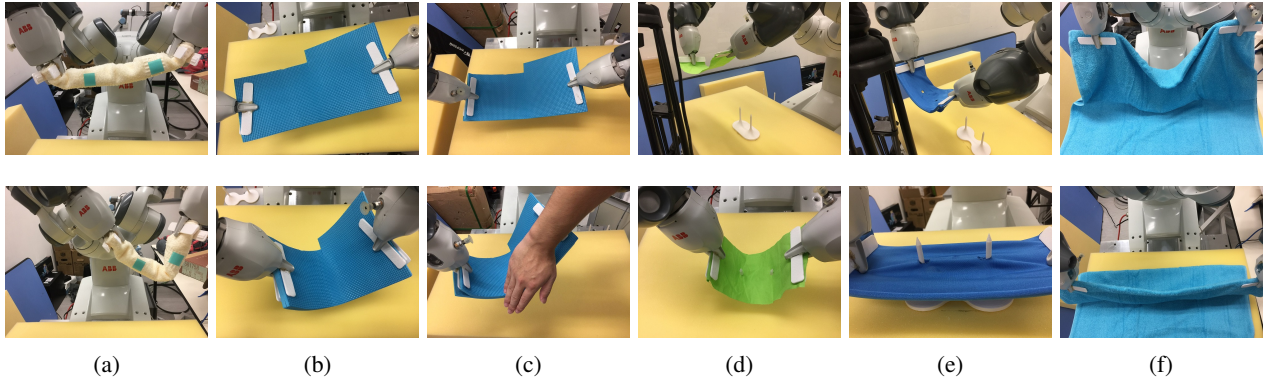


Fig. 11: The set of tasks used to evaluate the performance of the GPR-based nonlinear DOM controller: (a) rolled towel bending, (b) plastic sheet bending, (c) plastic sheet bending with occlusion, (d) peg-in-hole for unstretchable fabric, (e) peg-in-hole for stretchable fabric, and (f) towel folding. The first row shows the initial state of each object before the manipulation and the second row shows the goal states of the object after the successful manipulation.

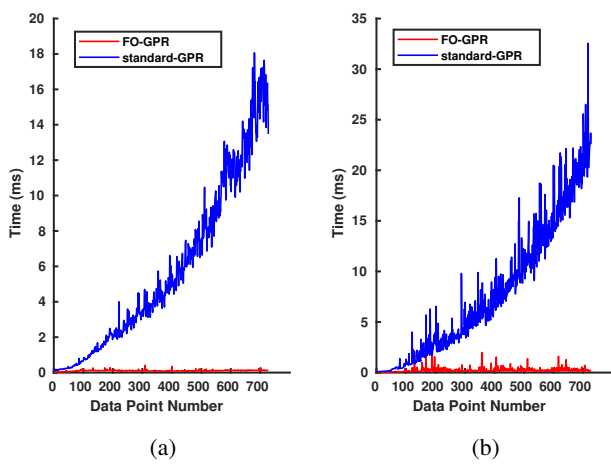


Fig. 12: Comparison of the time cost of FO-GPR and standard GPR: (a) the time cost comparison between GP model estimation; (b) the time cost comparison for the entire manipulation process.

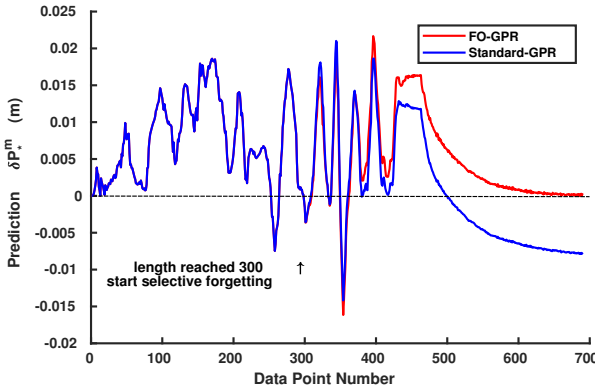


Fig. 13: Impact of selective forgetting in FO-GPR: FO-GPR is superior over the standard GPR in terms of the computational cost and the deformation model accuracy.

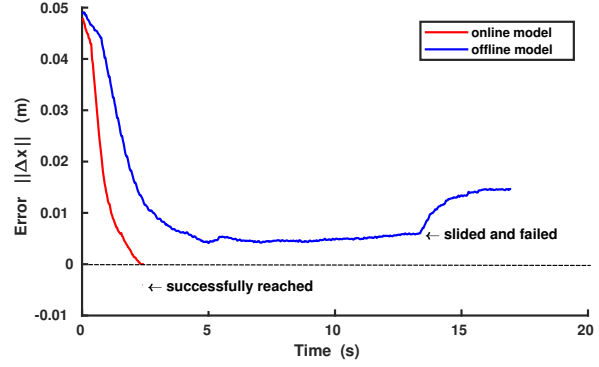


Fig. 14: Comparison of online and offline GP models for rolled towel manipulation. The controller based on the online model succeeds while the controller based on the offline model fails.

significantly, which can be 10 times slower than our FO-GPR based manipulation, whose time cost is always below 5 ms and allows for real-time manipulation. This experiment is performed using the rolled towel bending task.

2) *Impact of selective forgetting:* In Figure 13, we compares the GP prediction quality between FO-GPR and the standard GPR on the rolled towel task, in order to show the impact of selective forgetting in FO-GPR. We record about 700 data entries continuously. The first 450 data are produced using random controller, and the rest are generated by the FO-GPR based controller which drives the soft object toward the target state smoothly. Before the data size reaches the maximum limit  $M = 300$ , the controllers using two GPR models provide the same velocity output. From this point on, FO-GPR selectively forgets uninformative data while the standard GPR still uses all data for prediction. For data points with indices between 300 and 450, the output from two controllers are similar, which implies that FO-GPR still provides a sufficiently accurate model. After that, the FO-GPR based controller drives the object toward goal and eventually the controller output is zero; while for standard GPR, the controller output remains nonzero. This experiment suggests that the performance of FO-GPR is much better than the GPR in real applications in terms of both time saving and

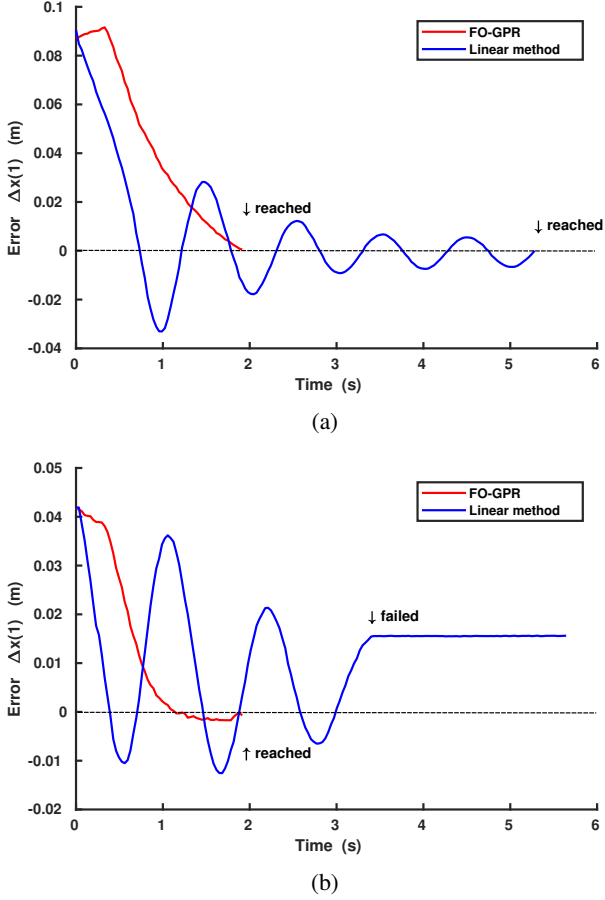


Fig. 15: Comparison of the controllers based on FO-GPR and the linear model: (a) comparison on the rolled towel task; (b) comparison on the peg-in-hole task with stretchable fabric.

the accuracy of the learned deformation model.

3) *Comparison of online and offline GPR*: In this experiment, we fix the Gram matrix unchanged after a while in the rolled towel manipulation task, and compare the performance of the resulting offline model with that of our online learning approach. As shown in Figure 14, the error in the feature space  $\|\Delta s\|_2$  decreases at the beginning of manipulation while using both models for control. However, when the soft object is close to its target configuration, the controller using the offline model cannot output accurate prediction due to the lack of data around the unexplored target state. Thanks to the balance of exploration and exploitation of online FO-GPR, our method updates the deformation model all the time and thus is able to output a relative accurate prediction so that the manipulation process is successful.

4) *Comparison of FO-GPR and adaptive Jacobian-based method*: We compare our approach to the state-of-the-art adaptive Jacobian-based method for soft object manipulation [18], which learns the Jacobian matrix using squared error function and stochastic gradient descent (SGD). Their method can be considered as a special case of our approach, where the deformation function is restricted to a linear function. First, through experiment we find that the learning rate of the linear model has a great impact on the manipulation

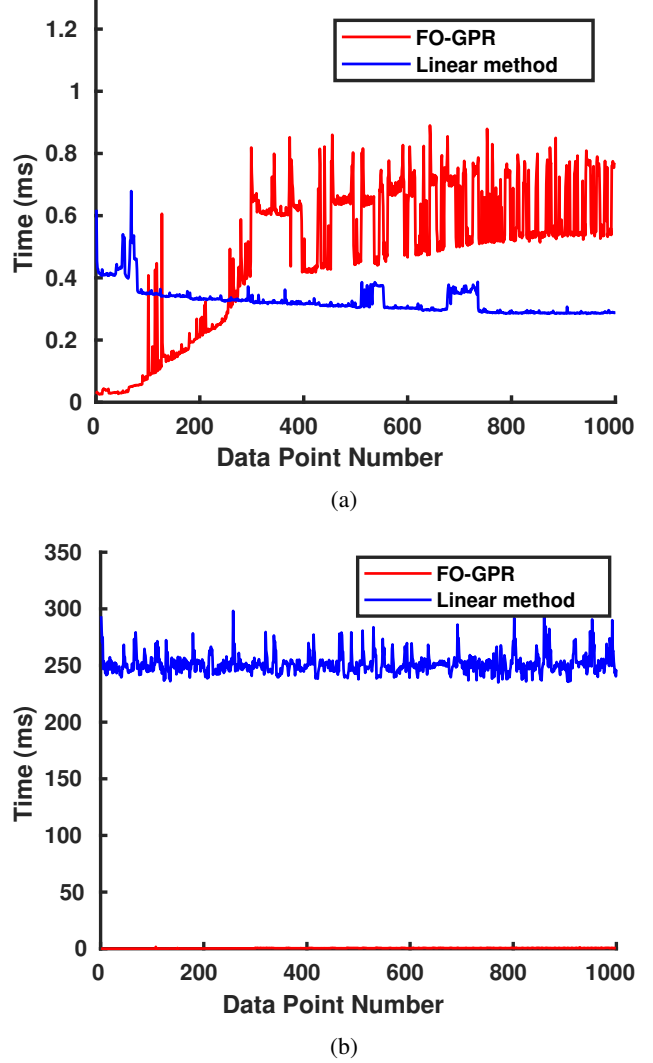


Fig. 16: Comparison of the time cost of FO-GPR and linear model on the rolled towel task (a) and the plastic sheet bending task (b).

performance and needs to be tuned offline for different tasks; while our approach is able to use the same set of parameters for all tasks. Next, we perform both methods on the rolled towel and the peg-in-hole with stretchable fabric tasks, and the results are shown in Figure 15a and 15b, respectively. To visualize the comparison results, we choose one dimension from the feature vector  $s$  and plot it. In Figure 15a, we observe that the error of the controller based on the linear model decreases quickly, but the due to the error in other dimensions the controller still outputs a high control velocity and thus vibration starts. The controller needs a long time to accomplish the task. As a contrast, the error of the plotted dimension decreases slower but the controller finishes the task faster because the error of all dimensions declines to zero quickly, thanks to the nonlinear modeling capability of GPR. In the peg-in-hole task, we can observe that the GPR-based controller successfully accomplish the task while the controller based on the linear model fails. We also compare the computational time of both methods in Figure 16. For

the rolled tower task, the adaptive-Jacobian based method is slightly (about 0.4 ms) faster than our approach since there are only 2 feedback points per frame. For the plastic sheet bending task with around 1200 feedback points per frame, the adaptive-Jacobian based method is significantly slower due to the expensive matrix multiplication while computing the gradient.

5) *Robustness to occlusion*: Our method is robust to moderate level of occlusions as shown in Figure 11c and 11f. Thanks to the online learning mechanism, our controller is able to output correct prediction for an occluded point once it has been observed before and thus has been learned by the GPR model. Nevertheless, our method may not provide correct prediction and the controller may fail if the occluded part changes significantly and the features change rapidly.

### C. Random forest-based DOM controller

Here we demonstrate the performance of random forest-based DOM controller on both simulated environment and real robot hardware. For the simulated environment, the robot’s kinematics are simulated using Gazebo [78] and the cloth dynamics are simulated using ArcSim [79], a high-accuracy cloth simulator. We use OpenGL to capture RGB-D in this simulated environment. For the real robotic environment, we use the same setup as before i.e., a RealSense depth camera to capture 640x480 RGB-D images and a 14-DOF ABB YuMi dual-armed manipulator to perform actions. Here the deformable object to be manipulated is restricted to a 35cm×30cm rectangular-shaped piece of cloth, as shown in Figure 17.

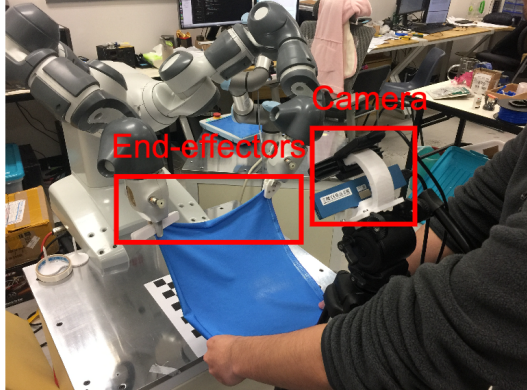


Fig. 17: Setup for random forest-based DOM controller: A dual-armed robot and a human are holding four corners of the cloth. We use an 14-DOF dual-armed ABB YuMi and an RealSense RGB-D camera to perform complex manipulation tasks. Our goal is to manipulate a 35cm×30cm rectangular-shaped piece of cloth.

Our goal is to manipulate a rectangular piece of cloth with four corners initially located at:  $v^0 = (0, 0, 0)$ ,  $v^1 = (0.3, 0, 0)$ ,  $v^2 = (0, 0.35, 0)$ ,  $v^3 = (0.3, 0.35, 0)$ (m). Our manipulator holds the first two corners,  $v^0, v^1$ , of the cloth and the environmental uncertainty is modeled by having a human holding the last two corners,  $v^2, v^3$ , of the cloth, so that we have  $\mathbf{r} \triangleq \begin{pmatrix} v^0 \\ v^1 \end{pmatrix}$  and each control action is 6-

dimensional. The human could move  $v^2, v^3$  to an arbitrary location under the following constraints:

$$0m < \|v^2 - v^3\| \leq 0.3m \quad (45)$$

$$\left\| \begin{pmatrix} v^2 \\ v^3 \end{pmatrix}_{i+1} - \begin{pmatrix} v^2 \\ v^3 \end{pmatrix}_i \right\|_\infty < 0.1(m/s), \quad (46)$$

where the first constraint avoids tearing the cloth apart and the second constraint ensures that the speed of human hand is slow.

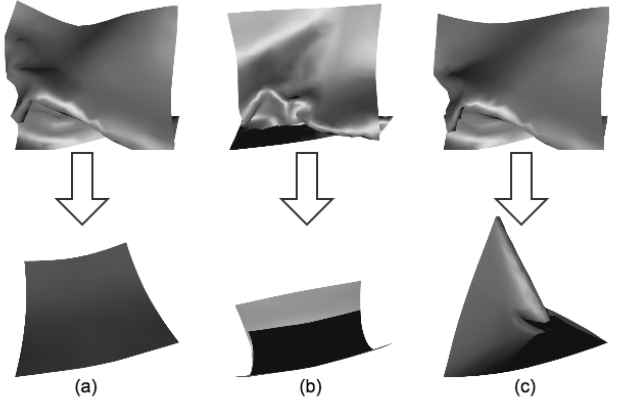


Fig. 18: Synthetic benchmarks: We highlight the real-time performance of the random-forest based controller on three tasks for the robot in simulator (a) keep the cloth straight, (b) keep the cloth bent, (c) keep the cloth twisted.

1) *Synthetic benchmarks*: To evaluate the robustness of our method, we design three manipulation tasks listed below:

- Cloth should remain straight in the direction orthogonal to human hands. This is illustrated in Figure 18 (a). Given  $v^2, v^3$ , the robot’s end-effector should move to:

$$v^0 = v^2 + 0.35 \frac{z \times (v^3 - v^2)}{\|z \times (v^3 - v^2)\|}, \quad (47)$$

$$v^1 = v^3 + 0.35 \frac{z \times (v^3 - v^2)}{\|z \times (v^3 - v^2)\|}. \quad (48)$$

- Cloth should remain bent in the direction orthogonal to human hands. This is illustrated in Figure 18 (b). Given  $v^2, v^3$ , the robot’s end-effector should move to:

$$v^0 = v^2 + 0.175 \frac{z \times (v^3 - v^2)}{\|z \times (v^3 - v^2)\|}, \quad (49)$$

$$v^1 = v^3 + 0.175 \frac{z \times (v^3 - v^2)}{\|z \times (v^3 - v^2)\|}. \quad (50)$$

- Cloth should remain twisted along the direction orthogonal to human hands. This is illustrated in Figure 18 (c). Given  $v^2, v^3$ , the robot’s end-effector should move to:

$$v^0 = v^3 + 0.175 \frac{z \times (v^3 - v^2)}{\|z \times (v^3 - v^2)\|}, \quad (51)$$

$$v^1 = v^2 + 0.175 \frac{z \times (v^3 - v^2)}{\|z \times (v^3 - v^2)\|}. \quad (52)$$

The above formula for determining  $v^0, v^1$  is used to simulate an expert. These three equations assume that the expert knows the location of the human hands, but that robot does not have this information and it must infer this latent information from a single-view RGB-D image of the current cloth configuration.

*2) Transferring from simulated environment to real robot hardware:* To transfer the controller parametrization trained on the synthetic data, we perform the following procedures. First, we use the camera calibration techniques to get both the extrinsic and intrinsic matrix of the RealSense Camera. Second, we compute the camera position, camera orientation, and the clipping range of the simulator from the extracted parameters. Third, we generate synthetic depth map using these parameters and train three tasks described in Section VIII-C.1 using the random forest-based controller parametrization along with the IL algorithm. After that, we integrate the resulting controller with the ABB YuMi dual-armed robot and the RealSense camera via ROS platform. As shown in Figure 19, with these identified parameters, we can successfully perform the same tasks as the synthetic benchmarks on the real robot platform.

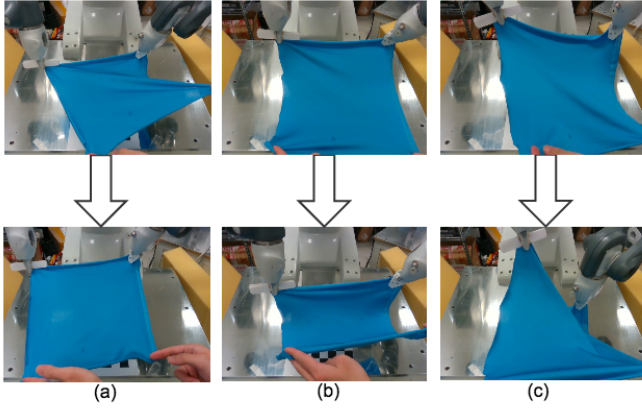


Fig. 19: Real robot manipulation benchmarks: We highlight the real-time performance of random forest-based DOM controller on three tasks for the robot and human collaboration (a) keep the cloth straight, (b) keep the cloth bent, (c) keep the cloth twisted.

*3) Performance:* To evaluate the performance of each component in the random forest-based DOM controller, we run several variants of Algorithm 4. All the meta-parameters used for training are illustrated in Table IV. In our first set of experiments, we train a single-task random forest-based controller for each task. We profile the mean action error:

$$\text{err} = \sum_{(\mathcal{O}(c), \mathbf{r}^*)} \frac{1}{|\mathbf{r}^*||\mathcal{D}|} \|\mathbf{r}^* - \frac{1}{K} \mathbf{r}_{l_k(\mathcal{O}(c)), k}^*\|^2, \quad (53)$$

with respect to the number of IL iterations (Line 0 of Algorithm 4).

As illustrated in Figure 21 (red), the action error reduces quickly within the first few iterations and converge later. We also plot the number of leaf-nodes in our random forest in Figure 21 (green). As our controller converges, our random

Name	Value
Fraction term used in IL algorithm [54]	0.8
Training data collected in each IL iteration	500
Resolution of RGB-D image	640 × 480
Dimension of HOW-feature used in Section V	768
Random forest's stopping criterion when impurity decrease less than [74]	$1 \times 10^{-4}$
L1 regularization weights, $\theta$ , in Equation 44	$1 \times 10^{-5}$

TABLE IV: Meta-parameters used for training.

forest's topology also converges. We have also tried to the construction of the random forest (Line 14 of Algorithm 4) from the IL algorithm, i.e. we construct random forest during the first iteration and then keep it fixed, only learning the optimal control actions using IL. As illustrated in Figure 21 (blue), the residual in the precluded version is larger than that in the original version. These experiments show that IL is suitable for training our random forest-based controller and allowing the random forest construction to be integrated into the IL algorithm does help improve controller performance. We also highlight the robustness of our method by comparing the performance of our controller with the basic controller using HOW features (Section V) in Figure 20. This is done by applying both controllers to a scenario with randomized human actions.

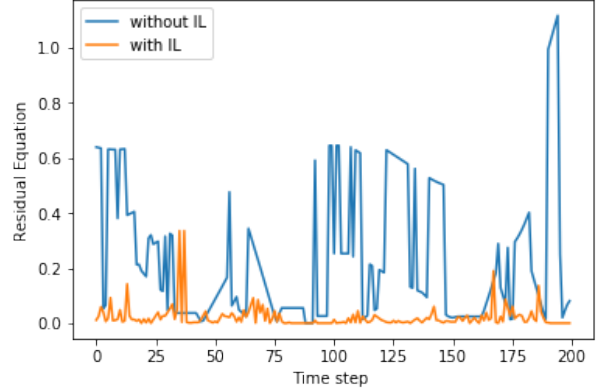


Fig. 20: Robustness of the imitation learning algorithm: In a real-time human robot interaction, we plot the mean action error (Equation 53). The blue curve shows the performance of controller which is trained using only one IL iteration and the orange curve shows the performance of controller with 20 IL iterations. We compare residual (Equation 53) between the two methods. The figure shows the robustness of the our method over the basic DOM controller using HOW features.

In our second experiment, we test the performance of the single-task controller, i.e. controller that is trained for a single manipulation task such as bending. In our simulated environment, this can be performed by running our simulator. During each simulation, we have the hands moving to 10 random target positions  $v^{2*}, v^{3*}$ . As shown in Figure 22(red), we profile the residual (Equation 53) in all 10 problems. Our controller performs consistently well with a relative action error of 0.4954%.

In the third experiment, we train a joint 3-task controller

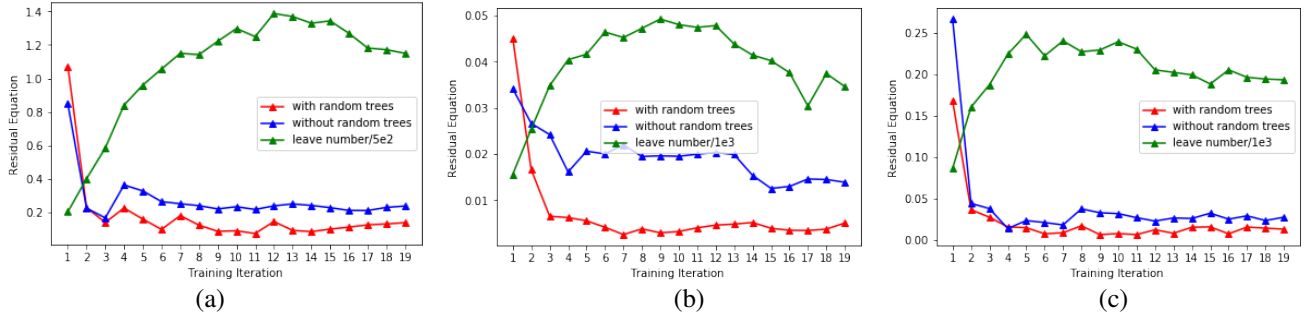


Fig. 21: Controller with Random-Forest v.s Controller without Random-Forest: (red): Residual (Equation 53) plotted against the IL iterations (Line 0 of Algorithm 4). (green): Number of leaf-nodes plotted against the IL iterations. (blue): Residual Equation 53 plotted against the IL iterations, which precludes random forest construction. (a): cloth straight; (b): cloth bent; (c): cloth twisted. As our controller converges, our random forests topology also converges. Our random-forest-based controller outperforms the previous method.

for all tasks. This is done by defining a single random forest and defining 3 optimal actions on each leaf-node. The performance of the 3-task controller is compared with the single-task controller in Figure 22. The multi-task controller performs slightly worse in each task, but the difference is quite small.

#### D. Benefits over prior approaches

A key feature of our method is that it allows the robot to react to random human movements, while the effect of these movements is indirectly reflected via a piece of cloth. This setting is very similar to [35]. However, [35] assumes the 3D cloth mesh  $c$  is known without sensing error, which is not practical.

Our method falls into a broader category of the visual-servoing methods, but most previous work in this area such as [80] focused on navigation tasks and there is relatively little work on deformable body manipulation. [58] based their servoing engine on histogram features which is a similar method to our HOW-feature. However, they use direct optimization to minimize the cost function ( $\text{dist}(\mathcal{O}(c), \mathcal{O}(c^*))$ ) which is not possible in our case because our cost function is non-smooth in general.

Finally, our method is closely related to [46], [53], which also use random forest and store actions on the forest. However, our method is different in two ways. First, our controller is continuous in its parameters, which means it can be trained using IL algorithm. We put both feature extraction and controller parametrization into the IL algorithm [54] so that both the feature extractor and the controller benefit from evolving training data.

## IX. CONCLUSION AND FUTURE WORK

We have presented a general approach framework to automatically servo-control soft objects using a dual-arm robot, and provide new solutions in both the feature design and the controller optimization. For feature design, we present a new algorithm to compute HOW-features, which capture the shape variation and local features of the deformable material using limited computational resources. The visual feedback dictionary is precomputed using sampling and clustering techniques and used with sparse representation

to compute the velocity of the controller to perform the task. For controller design, we first propose an online GPR model to estimate the deformation function of the manipulated objects, and used low-dimension features to describe the object's configuration. The resulting GPR-based visual servoing system can generate high quality control velocities for the robotic end-effectors and is able to accomplish a set of manipulation tasks robustly. We also present a DOM controller where the optimal control action is defined on the leaf-nodes of a random forest. Further, both the random forest construction and controller optimization are integrated with an imitation learning algorithm and evolved with training data. We evaluate our proposed approaches on a set of DOM benchmark tasks. The result shows that our method can seamlessly combine feature extraction and controller parametrization problems. In addition, our method is robust to random noises in human motion and can accomplish high success rate.

Our approaches have some limitations and there are many avenues for future work.

For the HOW feature design, since HOW-features are computed from 2D images, the accuracy of the computations can also vary based on the illumination and relative colors of the cloth. For future work, we would like to make our approach robust to the training data and the variation of the environment.

For the GPR-based DOM controller, the deformation function actually depends not only on the feature velocity but also on the current state of the object in some complicated manipulation tasks. i.e., the input of the deformation function should add a variable to represent current state, like relative positions of feedback or manipulated points. However that function is relatively difficult to learn by online exploration since the model needs more data. For future work, we plan to find a better exploration method to learn a more complicate deformation function involving not only the feature velocity but also the current configuration of the object in the feature space, in order to achieve more challenging tasks like cloth folding.

For the random forest-based DOM controller, it is not easy to extend our method to reinforcement learning scenarios.

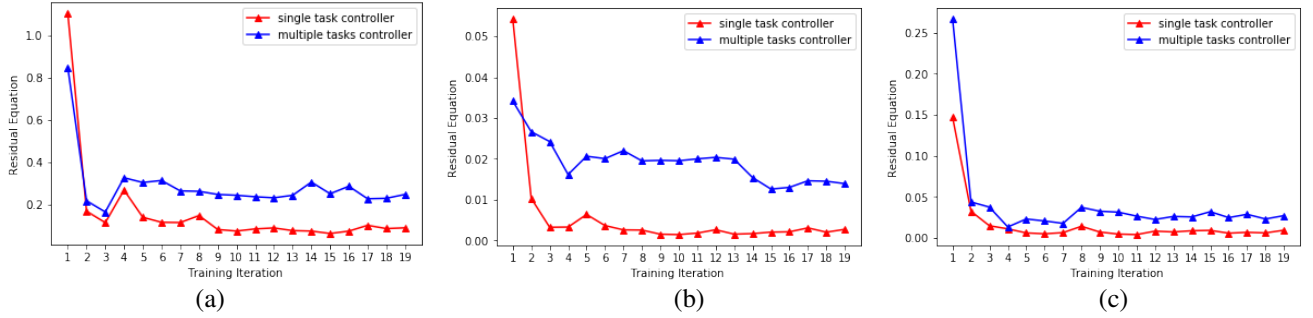


Fig. 22: Multi-task controller vs. single-task controller: Residual (Equation 53) in 10 random problems using joint 3-task controller (blue) and single-task controller (red). (a): cloth straight; (b): cloth bent; (c): cloth twisted. Both controller converges after a few iterations of IL algorithm. Especially, the single-task controller performs consistently well with a relative action error of 0.4954%. The multi-task controller performs slightly worse in each task, but the difference is relatively small.

This is because our method is not differentiable by involving a random forest construction. Therefore, reinforcement learning algorithms such as the policy gradient method [81] cannot be used. Another potential drawback is that our method is still sensitive to the random forest's stopping criterion. When the stopping criterion is too loose, the number of leaf-nodes can increase considerably, leading to overfitting in Equation 44. Finally, we need additional dimension reduction, i.e. the HOW-feature, and action labeling in the construction of the random forest. In our current version, labeling is done by mean-shift clustering of optimal actions, but in some applications, where observations can be semantically labeled, labeling observations instead of actions can be advantageous. For example, in object grasping tasks, we can construct our random forest to classify object types instead of classifying actions.

## REFERENCES

- [1] S. Miller, J. van den Berg, M. Fritz, T. Darrell, K. Goldberg, and P. Abbeel, "A geometric approach to robotic laundry folding," *The International Journal of Robotics Research*, vol. 31, no. 2, pp. 249–267, 2011.
- [2] M. Cusumano-Towner, A. Singh, S. Miller, J. F. O'Brien, and P. Abbeel, "Bringing clothing into desired configurations with limited perception," in *IEEE International Conference on Robotics and Automation*, 2011, pp. 3893–3900.
- [3] A. Kapusta, W. Yu, T. Bhattacharjee, C. K. Liu, G. Turk, and C. C. Kemp, "Data-driven haptic perception for robot-assisted dressing," in *IEEE International Symposium on Robot and Human Interactive Communication*, 2016, pp. 451–458.
- [4] Y. Gao, H. J. Chang, and Y. Demiris, "Iterative path optimisation for personalised dressing assistance using vision and force information," in *IEEE/RSJ International Conference on Intelligent Robots and Systems*, 2016, pp. 4398–4403.
- [5] Y. Li, X. Hu, Y. Yue, E. Grinspun, and P. K. Allen, "Multi-sensor surface analysis for robotic ironing," in *IEEE International Conference on Robotics and Automation*, 2016, pp. 5670–5676.
- [6] L. Twardon and H. Ritter, "Interaction skills for a coat-check robot: Identifying and handling the boundary components of clothes," in *IEEE International Conference on Robotics and Automation*, 2015, pp. 3682–3688.
- [7] J. Schrimpf, L. E. Wetterwald, and M. Lind, "Real-time system integration in a multi-robot sewing cell," in *IEEE/RSJ International Conference on Intelligent Robots and Systems*, 2012, pp. 2724–2729.
- [8] W. Wang, D. Berenson, and D. Balkcom, "An online method for tight-tolerance insertion tasks for string and rope," in *IEEE International Conference on Robotics and Automation*, 2015, pp. 2488–2495.
- [9] S. Patil and R. Alterovitz, "Toward automated tissue retraction in robot-assisted surgery," in *IEEE International Conference on Robotics and Automation*, 2010, pp. 2088–2094.
- [10] J. Schulman, J. Ho, C. Lee, and P. Abbeel, "Generalization in robotic manipulation through the use of non-rigid registration," in *International Symposium on Robotics Research*, 2013.
- [11] D. Kruse, R. J. Radke, and J. T. Wen, "Collaborative human-robot manipulation of highly deformable materials," in *IEEE International Conference on Robotics and Automation*, 2015, pp. 3782–3787.
- [12] S. Levine, C. Finn, T. Darrell, and P. Abbeel, "End-to-end training of deep visuomotor policies," *Journal of Machine Learning Research*, vol. 17, no. 1, pp. 1334–1373, 2016.
- [13] V. Mnih, K. Kavukcuoglu, D. Silver, A. A. Rusu, J. Veness, M. G. Bellemare, A. Graves, M. Riedmiller, A. K. Fidjeland, G. Ostrovski, S. Petersen, C. Beattie, A. Sadik, I. Antonoglou, H. King, D. Kumaran, D. Wierstra, S. Legg, and D. Hassabis, "Human-level control through deep reinforcement learning," *Nature*, vol. 518, no. 7540, pp. 529–533, 2015.
- [14] Y. Li, Y. Yue, D. Xu, E. Grinspun, and P. K. Allen, "Folding deformable objects using predictive simulation and trajectory optimization," in *IEEE/RSJ International Conference on Intelligent Robots and Systems*, 2015, pp. 6000–6006.
- [15] D. McConachie and D. Berenson, "Bandit-based model selection for deformable object manipulation," in *Workshop on the Algorithmic Foundations of Robotics*, 2016.
- [16] L. Bodenhagen, A. R. Fugl, A. Jordt, M. Willatzen, K. A. Andersen, M. M. Olsen, R. Koch, H. G. Petersen, and N. Krger, "An adaptable robot vision system performing manipulation actions with flexible objects," *IEEE Transactions on Automation Science and Engineering*, vol. 11, no. 3, pp. 749–765, 2014.
- [17] D. Navarro-Alarcon, Y. H. Liu, J. G. Romero, and P. Li, "Model-free visually servoed deformation control of elastic objects by robot manipulators," *IEEE Transactions on Robotics*, vol. 29, no. 6, pp. 1457–1468, 2013.
- [18] D. Navarro-Alarcon, H. M. Yip, Z. Wang, Y. H. Liu, F. Zhong, T. Zhang, and P. Li, "Automatic 3-d manipulation of soft objects by robotic arms with an adaptive deformation model," *IEEE Transactions on Robotics*, vol. 32, no. 2, pp. 429–441, 2016.
- [19] J. D. Langsfeld, A. M. Kabir, K. N. Kaipa, and S. K. Gupta, "Online learning of part deformation models in robotic cleaning of compliant objects," in *ASME Manufacturing Science and Engineering Conference*, vol. 2, 2016.
- [20] M. J. Sullivan and N. P. Papanikopoulos, "Using active-deformable models to track deformable objects in robotic visual servoing experiments," in *IEEE International Conference on Robotics and Automation*, vol. 4, 1996, pp. 2929–2934.
- [21] D. Navarro-Alarcon and Y. H. Liu, "Fourier-based shape servoing: A new feedback method to actively deform soft objects into desired 2-d image contours," *IEEE Transactions on Robotics*, vol. 34, no. 1, pp. 272–279, 2018.
- [22] D. Hadfield-Menell, A. X. Lee, C. Finn, E. Tzeng, S. Huang, and P. Abbeel, "Beyond lowest-warping cost action selection in trajectory transfer," in *IEEE International Conference on Robotics and Automation*, 2015, pp. 3231–3238.

[23] T. Tang, C. Liu, W. Chen, and M. Tomizuka, "Robotic manipulation of deformable objects by tangent space mapping and non-rigid registration," in *IEEE/RSJ International Conference on Intelligent Robots and Systems*, 2016, pp. 2689–2696.

[24] P. C. Yang, K. Sasaki, K. Suzuki, K. Kase, S. Sugano, and T. Ogata, "Repeatable folding task by humanoid robot worker using deep learning," *IEEE Robotics and Automation Letters*, vol. 2, no. 2, pp. 397–403, 2017.

[25] A. Doumanoglou, J. Stria, G. Peleka, I. Mariolis, V. Petrak, A. Karakakos, L. Wagner, V. Hlav, T. K. Kim, and S. Malassiotis, "Folding clothes autonomously: A complete pipeline," *IEEE Transactions on Robotics*, vol. 32, no. 6, pp. 1461–1478, 2016.

[26] D. Tanaka, S. Arnold, and K. Yamazaki, "Emd net: An encode – manipulate – decode network for cloth manipulation," *IEEE Robotics and Automation Letters*, vol. 3, no. 3, pp. 1771–1778, 2018.

[27] D. Henrich and H. Wörn, *Robot manipulation of deformable objects*. Springer Science & Business Media, 2012.

[28] M. Saha and P. Isto, "Manipulation planning for deformable linear objects," *IEEE Transactions on Robotics*, vol. 23, no. 6, pp. 1141–1150, 2007.

[29] M. Moll and L. E. Kavraki, "Path planning for deformable linear objects," *IEEE Transactions on Robotics*, vol. 22, no. 4, pp. 625–636, 2006.

[30] Y. Bai, W. Yu, and C. K. Liu, "Dexterous manipulation of cloth," *Computer Graphics Forum*, vol. 35, no. 2, pp. 523–532, 2016.

[31] T. Matsuno, D. Tamaki, F. Arai, and T. Fukuda, "Manipulation of deformable linear objects using knot invariants to classify the object condition based on image sensor information," *IEEE/ASME Transactions on Mechatronics*, vol. 11, no. 4, pp. 401–408, 2006.

[32] M. Bell and D. Balkcom, "Grasping non-stretchable cloth polygons," *International Journal of Robotics Research*, vol. 29, no. 6, pp. 775–784, 2010.

[33] Y. Li, D. Xu, Y. Yue, Y. Wang, S. F. Chang, E. Grinspun, and P. K. Allen, "Regrasping and unfolding of garments using predictive thin shell modeling," in *IEEE International Conference on Robotics and Automation*, 2015, pp. 1382–1388.

[34] D. Berenson, "Manipulation of deformable objects without modeling and simulating deformation," in *IEEE/RSJ International Conference on Intelligent Robots and Systems*, 2013, pp. 4525–4532.

[35] S. Hirai and T. Wada, "Indirect simultaneous positioning of deformable objects with multi-pinch fingers based on an uncertain model," *Robotica*, vol. 18, no. 1, pp. 3–11, 2000.

[36] S. Rodriguez, J.-M. Lien, and N. M. Amato, "Planning motion in completely deformable environments," in *IEEE International Conference on Robotics and Automation*, 2006, pp. 2466–2471.

[37] B. Frank, C. Stachniss, N. Abdo, and W. Burgard, "Efficient motion planning for manipulation robots in environments with deformable objects," in *International Conference on Intelligent Robots and Systems*, 2011, pp. 2180–2185.

[38] K. B. Reed, A. Majewicz, V. Kallem, R. Alterovitz, K. Goldberg, N. J. Cowan, and A. M. Okamura, "Robot-assisted needle steering," *IEEE Robotics Automation Magazine*, vol. 18, no. 4, pp. 35–46, 2011.

[39] A. Clegg, J. Tan, G. Turk, and C. K. Liu, "Animating human dressing," *ACM Transactions on Graphics*, vol. 34, no. 4, pp. 116:1–116:9, 2015.

[40] J. Schulman, A. Lee, J. Ho, and P. Abbeel, "Tracking deformable objects with point clouds," in *IEEE International Conference on Robotics and Automation*, 2013, pp. 1130–1137.

[41] B. Wang, L. Wu, K. Yin, U. Ascher, L. Liu, and H. Huang, "Deformation capture and modeling of soft objects," *ACM Transactions on Graphics*, vol. 34, no. 4, pp. 94:1–94:12, 2015.

[42] I. Leizea, A. Mendizabal, H. Alvarez, I. Aguinaga, D. Borro, and E. Sanchez, "Real-time visual tracking of deformable objects in robot-assisted surgery," *IEEE Computer Graphics and Applications*, vol. 37, no. 1, pp. 56–68, 2017.

[43] R. A. Newcombe, D. Fox, and S. M. Seitz, "Dynamicfusion: Reconstruction and tracking of non-rigid scenes in real-time," in *IEEE Conference on Computer Vision and Pattern Recognition*, 2015, pp. 343–352.

[44] M. Innmann, M. Zollhöfer, M. Nießner, C. Theobalt, and M. Stamminger, "Volumedeform: Real-time volumetric non-rigid reconstruction," in *International Conference on European Conference on Computer Vision*, 2016, pp. 362–379.

[45] M. Dou, S. Khamis, Y. Degtyarev, P. Davidson, S. R. Fanello, A. Kowdle, S. O. Escalano, C. Rhemann, D. Kim, J. Taylor *et al.*, "Fusion4d: Real-time performance capture of challenging scenes," *ACM Transactions on Graphics*, vol. 35, no. 4, pp. 114:1–114:13, 2016.

[46] A. Doumanoglou, A. Kargakos, T. K. Kim, and S. Malassiotis, "Autonomous active recognition and unfolding of clothes using random decision forests and probabilistic planning," in *IEEE International Conference on Robotics and Automation*, 2014, pp. 987–993.

[47] P.-C. Yang, K. Sasaki, K. Suzuki, K. Kase, S. Sugano, and T. Ogata, "Repeatable folding task by humanoid robot worker using deep learning," *IEEE Robotics and Automation Letters*, vol. 2, no. 2, pp. 397–403, 2017.

[48] R. S. Sutton and A. G. Barto, *Introduction to Reinforcement Learning*, 1st ed. Cambridge, MA, USA: MIT Press, 1998.

[49] A. Hussein, M. M. Gaber, E. Elyan, and C. Jayne, "Imitation learning: A survey of learning methods," *ACM Computing Surveys*, vol. 50, no. 2, pp. 21:1–21:35, 2017.

[50] R. F. Stengel, *Stochastic Optimal Control: Theory and Application*. New York, NY, USA: John Wiley & Sons, Inc., 1986.

[51] A. X. Lee, S. H. Huang, D. Hadfield-Menell, E. Tzeng, and P. Abbeel, "Unifying scene registration and trajectory optimization for learning from demonstrations with application to manipulation of deformable objects," in *IEEE/RSJ International Conference on Intelligent Robots and Systems*, 2014, pp. 4402–4407.

[52] E. Todorov, T. Erez, and Y. Tassa, "MuJoCo: A physics engine for model-based control," in *IEEE/RSJ International Conference on Intelligent Robots and Systems*, 2012, pp. 5026–5033.

[53] A. Doumanoglou, T.-K. Kim, X. Zhao, and S. Malassiotis, *Active Random Forests: An Application to Autonomous Unfolding of Clothes*. Springer International Publishing, 2014, pp. 644–658.

[54] S. Ross, G. J. Gordon, and D. Bagnell, "A reduction of imitation learning and structured prediction to no-regret online learning," in *International Conference on Artificial Intelligence and Statistics*, G. J. Gordon and D. B. Dunson, Eds., vol. 15. Journal of Machine Learning Research - Workshop and Conference Proceedings, 2011, pp. 627–635.

[55] A. Gupta, C. Eppner, S. Levine, and P. Abbeel, "Learning dexterous manipulation for a soft robotic hand from human demonstrations," in *IEEE/RSJ International Conference on Intelligent Robots and Systems*, 2016, pp. 3786–3793.

[56] F. Chaumette and S. Hutchinson, "Visual servo control. i. basic approaches," *IEEE Robotics & Automation Magazine*, vol. 13, no. 4, pp. 82–90, 2006.

[57] S. Hutchinson, G. D. Hager, and P. I. Corke, "A tutorial on visual servo control," *IEEE transactions on robotics and automation*, vol. 12, no. 5, pp. 651–670, 1996.

[58] Q. Bateux and E. Marchand, "Histograms-based visual servoing," *IEEE Robotics and Automation Letters*, vol. 2, no. 1, pp. 80–87, 2017.

[59] R. B. Rusu, N. Blodow, and M. Beetz, "Fast point feature histograms (fpfh) for 3d registration," in *IEEE International Conference on Robotics and Automation*, 2009, pp. 1848–1853.

[60] D.-S. Lee, "Effective gaussian mixture learning for video background subtraction," *IEEE transactions on pattern analysis and machine intelligence*, vol. 27, no. 5, pp. 827–832, 2005.

[61] T. S. Lee, "Image representation using 2d gabor wavelets," *IEEE Transactions on pattern analysis and machine intelligence*, vol. 18, no. 10, pp. 959–971, 1996.

[62] J. G. Daugman, "Uncertainty relation for resolution in space, spatial frequency, and orientation optimized by two-dimensional visual cortical filters," *JOSA A*, vol. 2, no. 7, pp. 1160–1169, 1985.

[63] K. Yamazaki and M. Inaba, "A cloth detection method based on image wrinkle feature for daily assistive robots," in *IAPR Conference on Machine Vision Applications*, 2009, pp. 366–369.

[64] N. Dalal and B. Triggs, "Histograms of oriented gradients for human detection," in *IEEE Conference on Computer Vision and Pattern Recognition*, vol. 1, 2005, pp. 886–893.

[65] L. E. Baum, "An inequality and associated maximization technique in statistical estimation for probabilistic functions of markov process," *Inequalities*, vol. 3, pp. 1–8, 1972.

[66] J. A. Hartigan and M. A. Wong, "Algorithm as 136: A k-means clustering algorithm," *Journal of the Royal Statistical Society. Series C (Applied Statistics)*, vol. 28, no. 1, pp. 100–108, 1979.

[67] D. L. Donoho and M. Elad, "Optimally sparse representation in general (nonorthogonal) dictionaries via  $\ell_1$  minimization," *Proceedings of the National Academy of Sciences*, vol. 100, no. 5, pp. 2197–2202, 2003.

[68] E. Snelson and Z. Ghahramani, "Sparse gaussian processes using pseudo-inputs," in *Advances in neural information processing systems*, 2006, pp. 1257–1264.

- [69] C. E. Rasmussen and Z. Ghahramani, "Infinite mixtures of gaussian process experts," in *Advances in neural information processing systems*, 2002, pp. 881–888.
- [70] E. Snelson and Z. Ghahramani, "Local and global sparse gaussian process approximations," in *Artificial Intelligence and Statistics*, 2007, pp. 524–531.
- [71] D. Nguyen-Tuong, J. R. Peters, and M. Seeger, "Local gaussian process regression for real time online model learning," in *Advances in Neural Information Processing Systems*, 2009, pp. 1193–1200.
- [72] C. E. Rasmussen and C. K. Williams, *Gaussian processes for machine learning*. MIT press Cambridge, 2006, vol. 1.
- [73] J. R. Quinlan, "Induction of decision trees," *Machine learning*, vol. 1, no. 1, pp. 81–106, 1986.
- [74] J. Shotton, A. Fitzgibbon, M. Cook, T. Sharp, M. Finocchio, R. Moore, A. Kipman, and A. Blake, "Real-time human pose recognition in parts from single depth images," in *IEEE Conference on Computer Vision and Pattern Recognition*, 2011, pp. 1297–1304.
- [75] C. Zhu, R. H. Byrd, P. Lu, and J. Nocedal, "Algorithm 778: L-bfgs-b: Fortran subroutines for large-scale bound-constrained optimization," *ACM Transactions on Mathematical Software*, vol. 23, no. 4, pp. 550–560, 1997.
- [76] G. Biau, "Analysis of a random forests model," *Journal of Machine Learning Research*, vol. 13, no. 1, pp. 1063–1095, 2012.
- [77] P. Beeson and B. Ames, "TRAC-IK: An open-source library for improved solving of generic inverse kinematics," in *IEEE-RAS International Conference on Humanoid Robots*, 2015, pp. 928–935.
- [78] N. Koenig and A. Howard, "Design and use paradigms for gazebo, an open-source multi-robot simulator," in *IEEE/RSJ International Conference on Intelligent Robots and Systems*, vol. 3, 2004, pp. 2149–2154.
- [79] R. Narain, A. Samii, and J. F. O'Brien, "Adaptive anisotropic remeshing for cloth simulation," *ACM Transactions on Graphics*, vol. 31, no. 6, pp. 152:1–152:10, 2012.
- [80] A. X. Lee, S. Levine, and P. Abbeel, "Learning visual servoing with deep features and fitted q-iteration," 2017.
- [81] J. Peters and S. Schaal, "Policy gradient methods for robotics," in *IEEE/RSJ International Conference on Intelligent Robots and Systems*, 2006, pp. 2219–2225.